Cholinergic Wireless Photometry Device for Measurement of Neurontransmitter Markers in the Basal Forebrain and Hippocampus

A Thesis

Submitted to the Faculty

of the

WORCESTER POLYTECHNIC INSTITUTE

in partial fulfillment of the requirements for the

Degree in Master of Science

in

Electrical and Computer Engineering

by

Aatreya Chakravarti

Date of Submission: December 15, 2021

Professor Ulkuhan Guler

Professor John McNeill

Dr. Maysam Ghovanloo

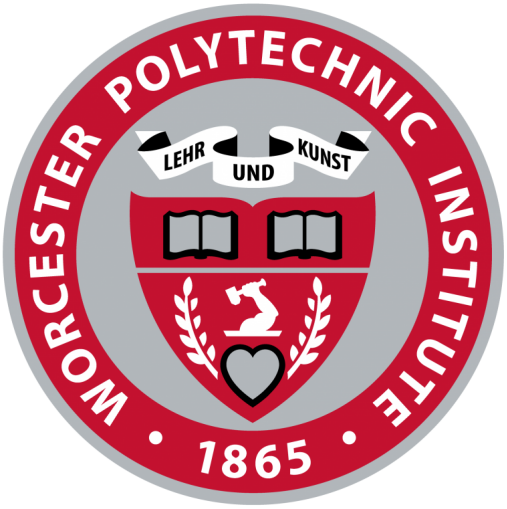

Worcester Polytechnic Institute

Primary Investigator: Professor Ulkuhan Guler

Cholinergic Wireless Photometry

By

Aatreya Chakravarti

December 15, 2021

Abstract

The growing population of elderly individuals in the last three decades has coincided with more patients suffering from neurological conditions. The result has been a marked decrease in quality of life for such patients. Studies have been conducted to identify the underlying biological mechanisms that lead to the onset of such disorders. The Cholinergic Hypothesis postulates that the disruption in the cholinergic neurotransmitter pathway explains progressive memory loss symptoms that manifest in many neurological diseases. Qualitative experiments observing animal model behavior have been conducted to verify this hypothesis. However, substantive quantitative data is lacking.

A quantitative method to measure neurological markers in the brain through optical stimulation and recording has become increasingly popular in the optogentic research space. This thesis presents prototype devices that are capable of using this method to measure cholinergic functionality. The presented devices put priority on distinct design specifications. In particular, the initial discrete-component prototype emphasized untethered device operation and multi-wavelength, multi-channel stimulation and recording. The second-iteration prototype converted the discrete-component circuits into a miniaturized integrated circuit capable of meeting the same specs. In addition, wireless power transfer and data telemetry functionality was developed. Simulation and in-vitro testing results act as a proof-of-concept for future in-vivo testing.

Acknowledgements

The completion of my research work would not have been accomplished without the sponsorship of the WPI Electrical and Computer Engineering Department as well as the Japan Agency for Medical and Research Development (AMED).

I would like to extend my sincerest appreciation to Professor Ulkuhan Guler for her support and technical guidance throughout the duration of my research. Her mentorship has without a doubt made me a better engineer.

I would also like to give a special thanks to Dr. Yusuke Tsuno. His neuroscience expertise filled a crucial knowledge gap which I have frequently benefited from during my research.

To the members of the Integrated Circuits and Systems (ICAS) lab, a special thanks for the good times spent together. I wish you all the best of luck in your future endeavours and hope we cross paths again in industry or elsewhere.

Finally, I would like to express my gratitude to my parents for their steadfast support throughout my academic career. During the most stressful period of my research, their constant encouragement made all the difference.

Contents

List of Figures

Chapter 1

Introduction

1.1 Motivation

According to United Nations, the percentage of the world population aged 65 and older has jumped from 5% in 1990 to ∼10% in 2020 [1]. The same source estimates that this number is going to increase to ∼18% by 2050.

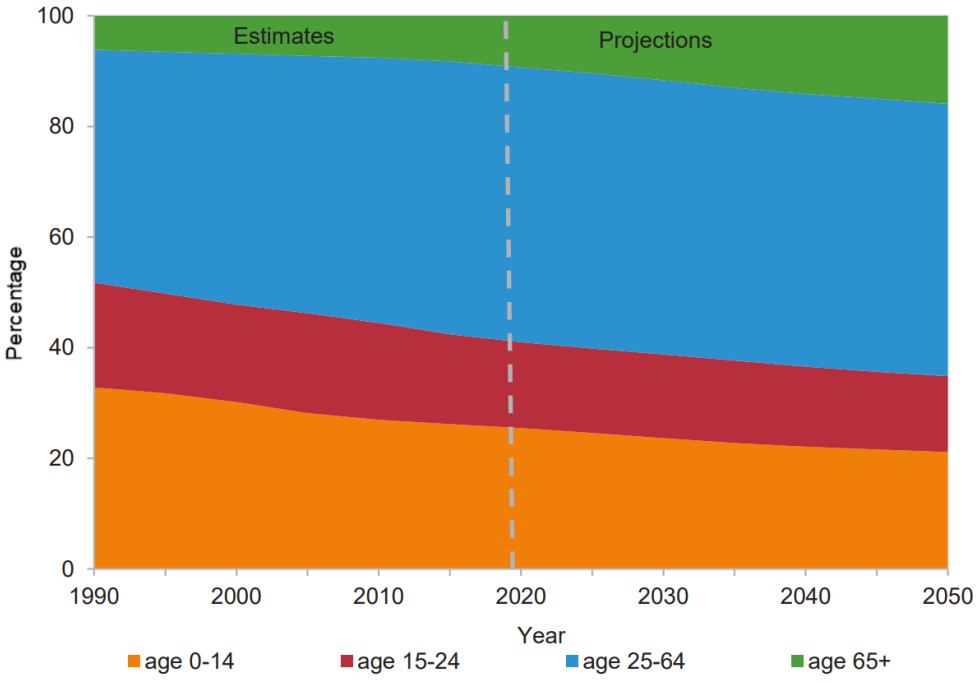

Figure 1.1: Global population trends by age groups from 2019 to 2050 [1].

With age comes higher susceptibility to developing neurological conditions such as Alzheimer's disease (AD), Parkinson's disease and Amyotrophic Lateral Sclerosis (ALS). According to a systematic review of data published in the 2021 Alzheimer's Association report, 6.2 million Americans aged 65 or older suffer from AD [7]. This data, further stratified by age, reveals a trend which correlates age with a higher AD prevalence. Of the number of Americans mentioned in the report, 27.6% are 65-74 years of age, 36.1% are 75-84 years of age, and 36.4% are 85+ years of age [7]. Similarly, a review of data from the Global Burden of Disease Study from 1990 through to 2016 found that the prevalence of Parkinson's disease exponentially increased for each 10-year age group. For individuals 30-40 years of age, the prevalence is 0.01% of the global population. This value increases to 0.33% for 60-70 years of age, 0.77% for 70-80 years of age, and peaking at 80-90 years of age, a prevalence of 1.37% [8]. Similar correlations between age and other neurological conditions have been found in data aggregation reports [9], [10].

Focusing on AD, the symptoms of this condition include social withdrawal in the early stage patients up to incontinence and primitive reflexes in late stage cases [11]. The effect on patients quality of life is significant and progressively worsens over time. Despite the evidence showing the correlation between age and cognitive decline, no cure for AD has been found due to a poor understanding of the mechanisms in the brain that lead to this and other neurological conditions. Attempting to further understand these mechanisms is the overarching motivation of this research work.

1.2 Cholinergic Hypothesis

Researchers have attempted to understand the mechanisms of AD and other neurological conditions by identifying common symptoms and working backwards. One such symptoms that is seen in nearly all AD patients is progressive memory loss and an inability to learn new information. The hippocampus, located in the medial temporal lobe of the brain, plays an

essential role in memory and learning [12]; therefore, many researchers have theorized that there is a link between degradation of the hippocampus and structures that feed into the hippocampus, such as the basal forebrain, and the symptoms of neurological conditions in aged individuals [13].

The 'Cholinergic Hypothesis', presented in 1982, explains the acceleration of memory loss in elderly individuals as a result of decline in cholinergic function [14]. Cholinergic dysfunction is defined as a disruption in the cholinergic neurotransmitter pathway indicated by low concentrations of various neurotransmitters and the elements that release these neurotransmitters [14]. More specifically, the basal forebrain production of acetylcholine (ACh),

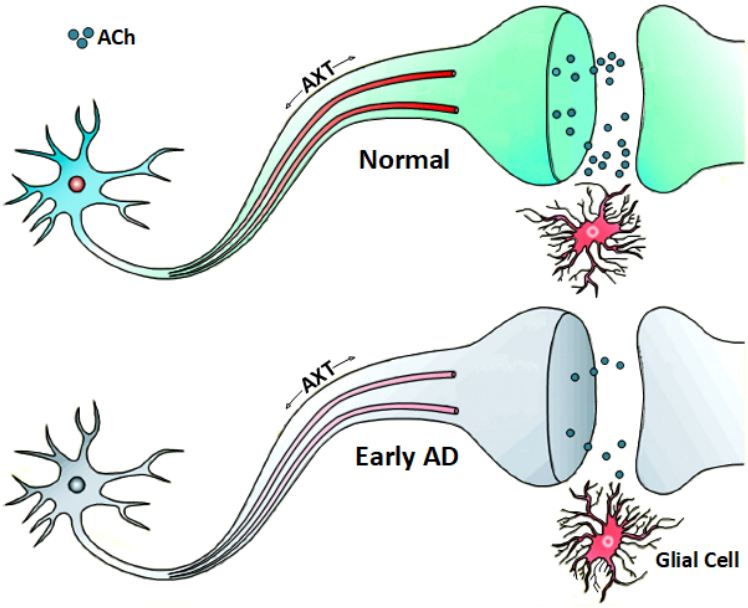

Figure 1.2: Illustration of cholinergic neurons in healthy versus early AD patients, influenced by [2].

a cholinergic neurotransmitter, has been experimentally shown in animal models to directly play a role in improving memory and learning in rats [15], [13]. In this study, researchers selected behaviorally impaired older rats and transplanted half of those rats with intrahippocampal cell suspension grafts that promote cholinergic neuron growth and ACh production. Both the experimental and control group rats were put in a maze and tested to see how long they would take to find the exit. The rats with transplanted cells demonstrated greater

spatial awareness and retention of the exit route on average compared to the control group suggesting a connection between ACh and cholinergic neuron degradation leading to memory loss symptoms.

While behavioral tests such as the ones done by [15], [13] provide qualitative evidence to substantiate the cholinergic hypothesis, the collection of quantitative data is much more conclusive in terms of experimental result replication as well as the elimination of confounding variables.

1.3 Previous Work

Many papers have been published that attempt to provide quantitative results to verify the cholinergic hypothesis through different methods. In following sections, the positive and negative aspects of different experimental techniques will be discussed.

1.3.1 Post-Mortem Analysis

Choline uptake and other cholinergic markers can be measured from the brain tissue of deceased patients who had AD. [16], [17] found that the concentration of choline acetyltranserase, an enzyme that catalyzes ACh, was consistently lower for AD patients as compared to non-AD patients. Post-mortem analysis provides quantitative data that circumvents the issues with the live animal behavioral tests mentioned earlier. However, neither the behavioral tests nor the post-mortem methods provide any information on the temporal dynamics in different time windows (seconds, minutes, days, weeks, and months) of cholinergic input and it's role in AD onset. These dynamics can be assessed with high temporal resolution in live animal models by directly measuring the hippocampal concentration of acetylcholine (ACh), a cholinergic neurotransmitter, in freely-moving animals, a method that will be explored next.

1.3.2 Indicator-enabled Optical Measurement

The continuous, real-time measurement of cholinergic element concentrations was enabled by the development of genetically-encoded indicators (GEI). These indicators modify neurons to fluoresce when cholinergic elements bond to them. When these modified neurons are stimulated with light, they in turn emit a light with an intensity proportional to the neurotransmitter element concentration in the environment around them. [18] designed an indicator that codes neurons in the basal forebrain to emit red light when calcium ions (Ca^{2+}), an element that triggers neurotransmitter release, docks to it. [19] created a similar indicator to make neurons in the hippocampus, where ACh is most commonly present, perform the same function. The response time of these sensors was empirically found to be $\sim$3 s allowing for detailed transient signal analysis [20]. An important characteristic of these sensor is that the wavelength of light is unique to stimulation and emission as well as between different sensors. For example, the Ca^{2+} GEI is stimulated by 560 nm light and encodes the neuron to emit 620 nm light, whereas the ACh GEI is stimulated by 470 nm light and the neuron emits 520 nm light. This detail allows for simultaneous optical stimulation and measurement of emissions of multiple neurotransmitter elements, a crucial feature of the devices discussed in later sections.

1.3.3 Fiber Photometry Devices

The current standard device used for optical stimulation and measurement are fiber photometry devices. [3], [21] are examples of such devices that perform neuron stimulation via an optical fiber inserted into the animals brain. The measurement of neuron response is done with electrodes, in the case of electrical readings, or a CMOS camera, in the case of optical emission measurements. This system provides reliable quantitative results, but comes with some drawbacks. Firstly, the use of an optical fiber for stimulation means that the animal is tethered to the laser source unit leading to unnatural subject behavior. Secondly, an optical fiber can only emit one wavelength of light at any time limiting experiments to single element

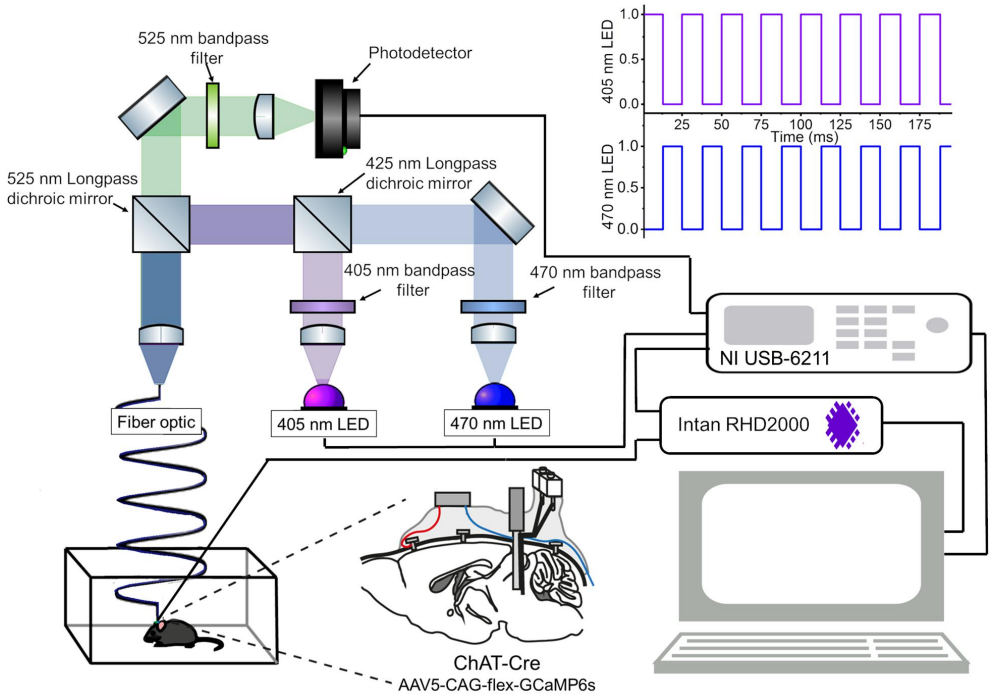

Figure 1.3: Illustration of fiber photometry system used in [3].

measurements. Multiple-wavelength stimulation requires more than one fiber which increases procedure invasiveness and can lead to increased abnormal animal subject behaviors.

1.3.4 Wireless Photometry Devices

Recent papers have attempted to address the challenges of legacy fiber photometry devices by designing miniaturized wireless devices that are capable of both stimulation and measurement of Ca^{2+} concentration. [4] presents a mm-sized implantable device that includes a headstage placed externally on the rat's scalp and an implantable stage surgically inserted underneath the skull. An intermediate coil located on the skull completes a three-coil system that provides wireless power from the headstage. Travelling in the other direction, backscatter on-off keying (OOK) modulation is used to send data to the headstage from the implantable circuit in a low-power fashion. Through this inductive link, one of the main limitations of fiber photometry systems is addressed. However, this and other optogenetic papers focus only on Ca^{2+} concentration measurement and do not explore ACh recording.

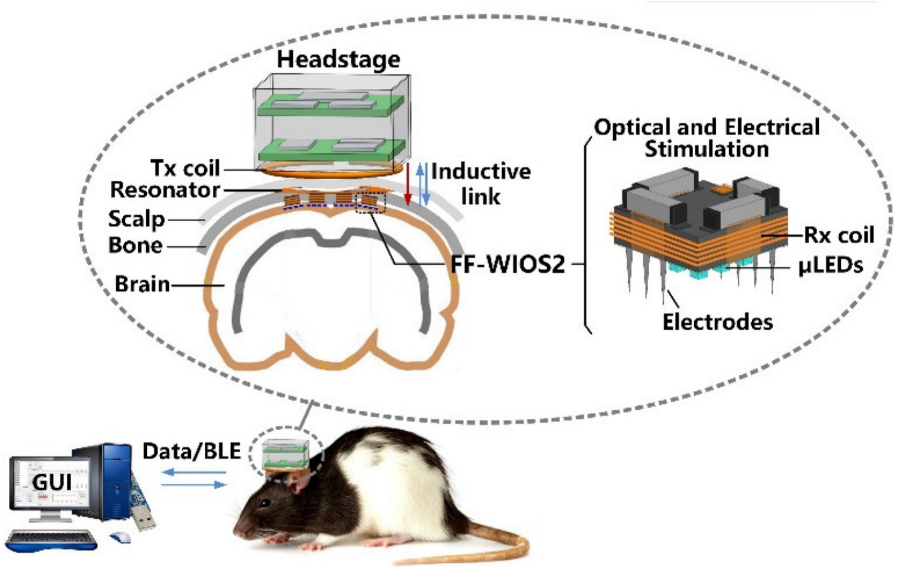

Figure 1.4: Illustration of mm-sized implantable photometry device presented in [4].

Kampasi et al. [5] looks into multi-wavelength recording by designing a device that uses waveguides to mix the light of two injection light diodes. This method of optical stimulation, as compared to the commonly used method of micro-light emitting diodes (μLEDs), allows multiple wavelengths of light from just two sources. The negative aspect of the this design choice is that multiple protrusions, refereed to as shanks, are required to deliver the light to the mouse's brain. In the paper, four shanks are present on the device resulting in four entry points in the brain which can be very invasive.

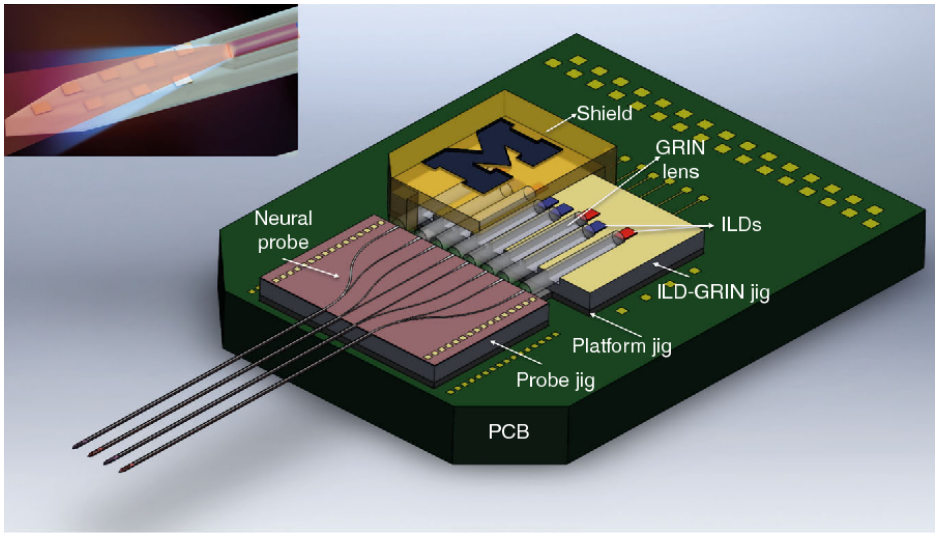

Figure 1.5: Illustration of multi-shank photometry device presented in [5].

1.4 Proposed Work

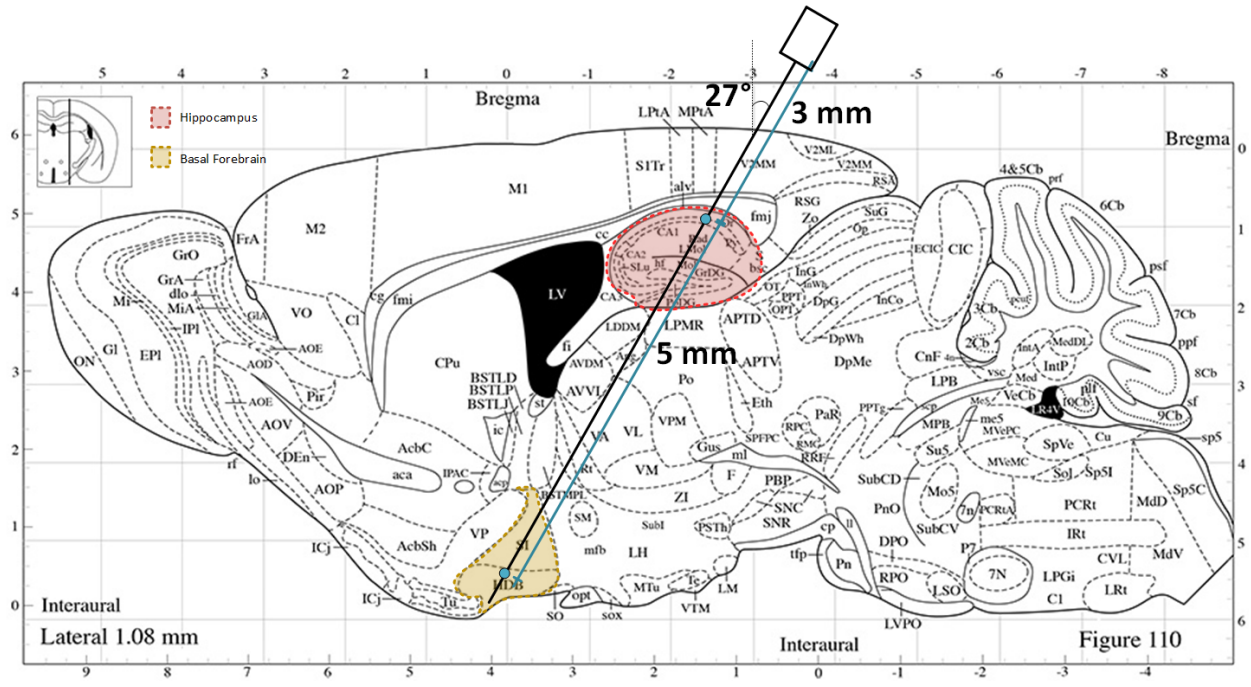

Figure 1.6: Illustration of shank positioning presented in [6].

This research is focused on designing a tri-color photometry system capable of optically stimulating and recording multiple wavelengths. To achieve this goal, the shank placement is an essential aspect of the design. To measure both ACh and Ca^{2+} in the hippocampus and basal forebrain, the shank will be inserted at approximately a 27° angle perpendicular to the surface of the animal's brain, as shown in Figure 1.6 (based on the Mouse Brain Atlas [22]).

The motivation for such a device in the long-run is decoding the human brain's underlying mechanisms that cause cognitive decline and a possibility to open up a new venue for surrogate methods that can provide noninvasive personalized monitoring of cognitive decline in patients, specifically in relation to the memory deficits and other cholinergic hippocampus-specific functions. More specifically, building the temporal profile of ACh and Ca^{2+} input simultaneously will help identify the relationship between cholinergic input and the magnitude of behavioral cognitive impairment. The data collected with this novel technology will provide a strong basis for uncovering the basic mechanism of cognitive decline in aging.

Section 2 will cover the first-iteration device design and results and Section 3 will repeat the process for the second-iteration prototype. Finally, Section 4 will conclude the research work completed and the future research topics to be explored.

Chapter 2

Photometry Device: Discrete Component Prototype

2.1 Design Goals

The purpose of an initial prototype for cholinergic sensing was to provide a proof-of-concept for the validity of simultaneous LED stimulation and measurement with off-the-shelf-components (COTS) prior to investing time and resources into a miniaturized, integrated circuit device solution. In addition, the expectation was to create preliminary results from in-vitro lab experimentation for the Human Frontiers Grant proposal. With these big-picture goals in mind, the design criteria for this device were:

(i) Simultaneous driving of three LEDs of different wavelengths

(ii) Simultaneous measurement of emitted light of different wavelengths

(iii) Untethered, COTS-design device

While device size and power consumption were minimized, ultimate miniaturization and very lower power operation were not the primary concerns of this first prototype.

2.2 Block Level System

As can be seen in Figure 2.1, the system contains an optical stimulation block to excite the neurons and an optical recording block to record the emitted light. For this prototype, three wavelengths of light are used for stimulation and two photodiodes are used for recording purposes. The three wavelengths of light cover stimulation of Ca^{2+}-docked neurons and ACh-docked neurons which are the cholinergic neurotransmitter markers discussed in the previous section. In addition, capability to measure an isobestic ACh (ACh_{iso}) is included. The isobestic signal does not vary with changes in ACh concentration; therefore, it is used as a reference level for post-measurement processing. For example, any DC drift will affect both the ACh and ACh_{iso} recordings equally. As a result, the DC component can be removed from the ACh signal by subtracting it with the ACh_{iso} signal.

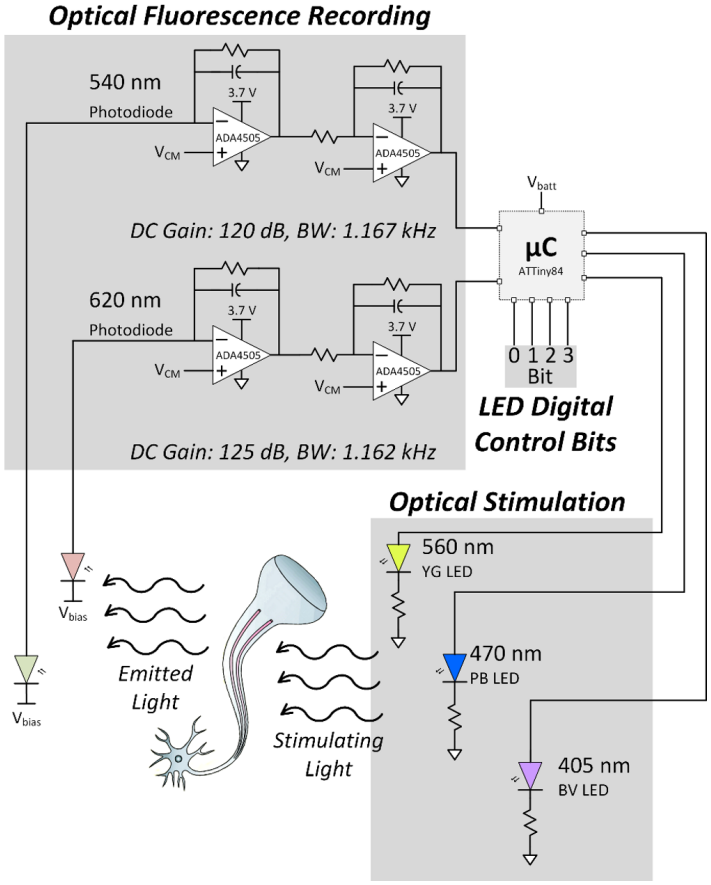

Figure 2.1: High-level illustration of system.

To minimize dark current, the photodiodes were reverse biased. The worst case dark current for both photodiodes according to their datasheets is 5 nA. This is significantly less than the photocurrent generated which is in the 1-3 uA range. Therefore, the effect of dark current-generated noise is minimal. Further noise analysis is presented in Section 2.4.3.

2.3 Optical Stimulation Block

2.3.1 System Design

In this block, the microcontroller (MCU) drives each of the LEDs so that the appropriate neurons can be stimulated and three signals can be recorded. The three signals and their stimulation and emission wavelengths are given below.

Table 2.1: Signals of Interest Stimulation and Emission Wavelengths

Neural Signal	**Stimulation Wavelength**	**Emission Wavelength**
Ca^{2+} Sensing	525-575 nm (yellow green)	620-660 nm (orange)
ACh Sensing	465-480 nm (pure blue)	510-530 nm (blue green)
ACh_{iso} Sensing	405 nm (blue violet)	510-530 nm (blue green)

A Microchip ATTiny84 MCU was chosen for this design. The justification for this component selection is as follows:

- Low profile quad-flat no-leads (QFN) package and small form factor of 4 x 4 mm
- Low active current of 300 μA and quiescent current of 0.1 μA
- On-board 10-bit ADC (acceptable for our output signal frequency)
- Input-Output (I/O) pins capable of sourcing up 40 mA of current

The LEDs are driven by PWM signals generated by the digital output pins of the MCU. Each of the LEDs are sourced by separate I/O pins to allow for design flexibility. The ACh and

ACh_{iso} signal emission are at the same wavelength, therefore they must be time-multiplexed so that the photodiode is able to distinguish between the two signals. The Ca^{2+} signal is spatially separated, but is also time-multiplexed to ensure limited emission interference.

The MCU is directly used to drive the LEDs as opposed to using a dedicated LED driver because the ATTiny84 can source up to 40 mA from each I/O pin. This well exceeds the 20 mA max current needed to drive each LED. In addition, using a separate LED driver chip would likely require an external oscillator that would be at a fixed frequency. Additional circuitry would be required to modulate the period and duty cycle of the LED driving signal. In contrast, the MCU can be easily programmed for varying periods and duty cycles with a resolution of 1 millisecond.

Finally, to control the illuminance of the LEDs, four bits have been allocated that can be set to a high (Vsupply) or low (ground) voltage. The corresponding four-bit binary code ranges from 0000 to 1111. The first two bits will be read by the MCU to select the LED (i.e. 00 is L1, 01 is L2, and 10 is L3). The last two bits will be used to set the brightness to four pre-defined levels. To ensure that the current flowing through the LED does not exceed the absolute maximum current rating, a discrete resistor is placed in series. The value of the resistor is calculated by taking the voltage drop across the LED given in the component datasheet.

$$R_{series} = \frac{V_{PWM} - V_{LED}}{I_{max}} \tag{2.1}$$

For the LED component selection, the main priority was matching the current sourcing requirements presented in optogentic papers [4], [23] that have done animal testing. This is of importance because these current sourcing requirements have been shown to produce the necessary optical power levels to stimulate the neurons. LED current requirements are dependent on the size and peak wavelength of the LED. In the optogenetic papers referenced earlier, bare LED dies (i.e. micro-LEDs with the packaging removed) were used to minimize surgical damage to the animal model when the components were inserted close to the neuron in the brain during in-vivo experimentation. Unfortunately, LED dies are expensive, sold in

large quantity, and are difficult to solder without precise micro-machine lab tools. Therefore, to mimic these components, packaged pico-LEDS (pLEDs) manufactured by ROhm were used. These pLEDS, despite their small form factor, generate comparable optical power to LED dies. In addition, the dimensions of the pLEDs is 0.6 x 1 mm which is the the smallest packaged LED that is commercially available as far as we know.

2.3.2 LED Driver Lab Measurements

As shown in Figure 2.1, the system is designed to simultaneously stimulate three LEDs. To ensure that there is no interference in emissions, the LED ON periods are equally time-multiplexed over an overall period of 150 ms. The LED current measurements were done by recording the voltage across a series sense resistor and calculating the current in post-processing.

As shown in Figure 2.2, the current for the 560 nm and 405 nm LEDs have a peak current of ∼20 mA which matches the requirements listed in the respective LED datasheets. Similarly, the 470 nm LED peak current of ∼5 mA is in line with the required current for maximum optical power emission.

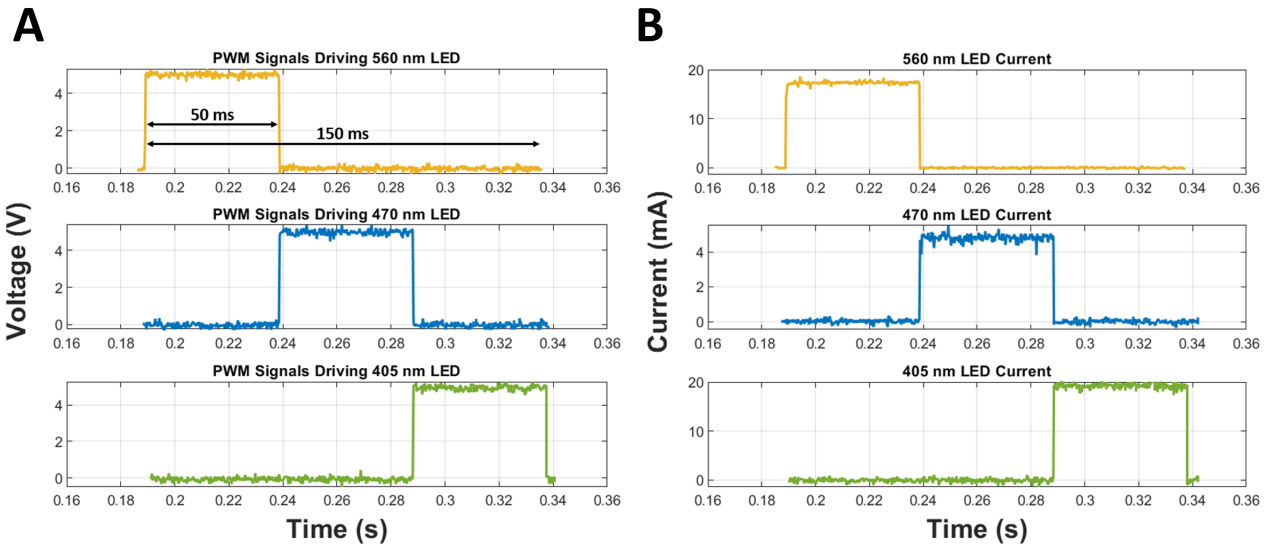

Figure 2.2: Lab measurement results of (A) PWM voltage signals driving LEDs. (B) LED current.

Measurements were also carried out to verify the linearity of user bit control of LED intensity. A Thorlabs Spectrometer was used to determine relative luminous intensity for each LED for increasing bit codes from 0000 to 0011. Figure 2.3 shows this plot for the 560 nm LED.

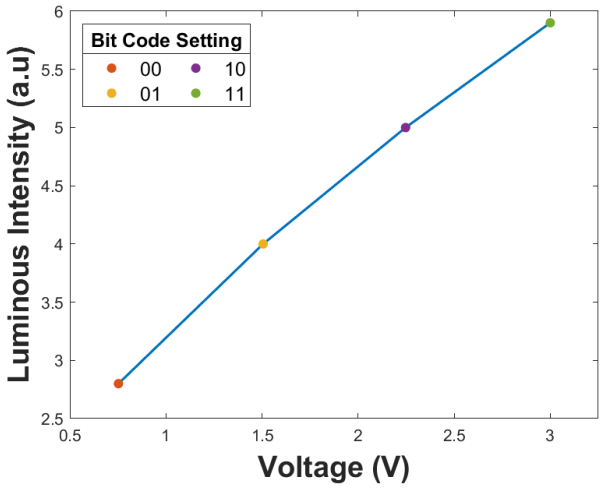

Figure 2.3: Lab measurement results of luminous intensity at different bit code values for the 560 nm LED.

2.4 Optical Recording Block

2.4.1 System Design

In this block, the current generated by the photodiodes is converted into voltage that can be sampled by the MCU. To achieve this conversion, a transimpedance amplifier (TIA) topology is used. A TIA has a shunt-shunt feedback structure with low input and output resistance. The combination of these two circuit features allows the output current to generate a measurable voltage across the output resistance of the amplifier. The theoretical closed-loop gain of a TIA can be calculated with a simplified amplifier model:

$$\frac{V_{out}(s)}{I_{in}(s)} = -R_f \cdot \left(\frac{A_{OL}}{1 + A_{OL} + \frac{sC_{in}R_f}{1+sC_fR_f}} \right) \tag{2.2}$$

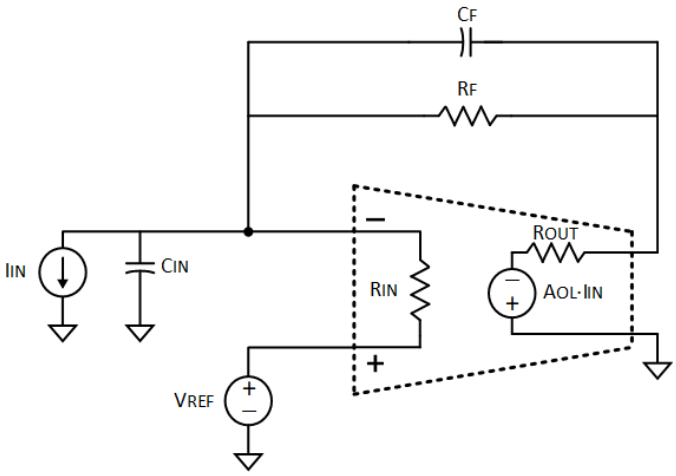

Figure 2.4: Simplified TIA model to calculate closed-loop gain.

Assuming a large open-loop gain (A_{OL}), the closed-loop gain can be approximated as follows:

$$\lim_{A_{OL}\to\infty} \frac{V_{out}(s)}{I_{in}(s)} \approx -R_f \tag{2.3}$$

As shown in Equation 2.4, the feedback resistor is the main factor in determining the gain which simplifies circuit design. One advantage of having a large feedback resistor is that the primary pole of the circuit is determined by the time constant formed by the two feedback elements. The bandwidth of the TIA is as follows:

$$BW = \frac{1}{2\pi C_f R_f} \tag{2.4}$$

To determine the required TIA specs for the photometry application, the input and desired output signal characteristics are important to define. Based on Fast Fourier Transform (FFT) of the data taken from fiber photometry studies by our collaborator at Kanazawa University, the main signal power ranges from 1-10 Hz with an amplitude of $\sim$17 μA.

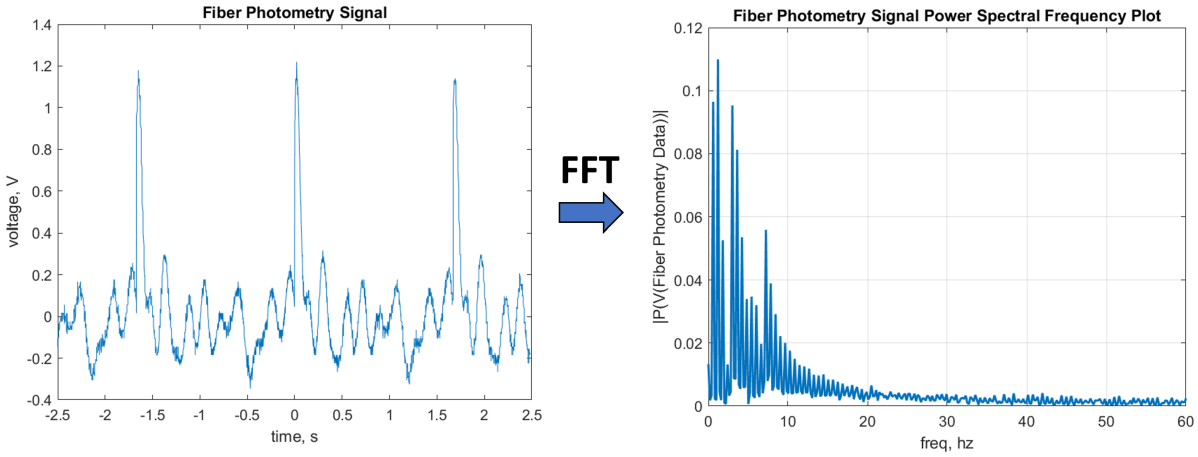

Figure 2.5: Spectral frequency plot of signals measured with fiber optic setup by our collaborator at Kanazawa University.

To account for worst-case scenario signal conditions, the input signal amplitude is taken to be 1 μA and the desired output signal amplitude is set to 1 V. Therefore, the required DC transimpedance gain is calculated as follows:

$$Gain = \frac{V_{out}}{I_{in}} = \frac{1V}{1\mu A} = 1M\Omega \quad (120dB) \tag{2.5}$$

To implement a TIA circuit for the design specifications listed above, a two-stage circuit was selected. The first stage provides the gain and the second stage sets the bandwidth. Based on the gain and bandwidth equations given earlier in the section, the gain for the 520 nm and 620 nm photodiodes was set to 120 dB and 125 dB respectively. The difference in gains accounts for the fact that the 520 nm photodiode produces less photocurrent compared to the 620 nm photodiode at the same illuminance. The bandwidths were set to 1.167 kHz and 1.162 kHz.

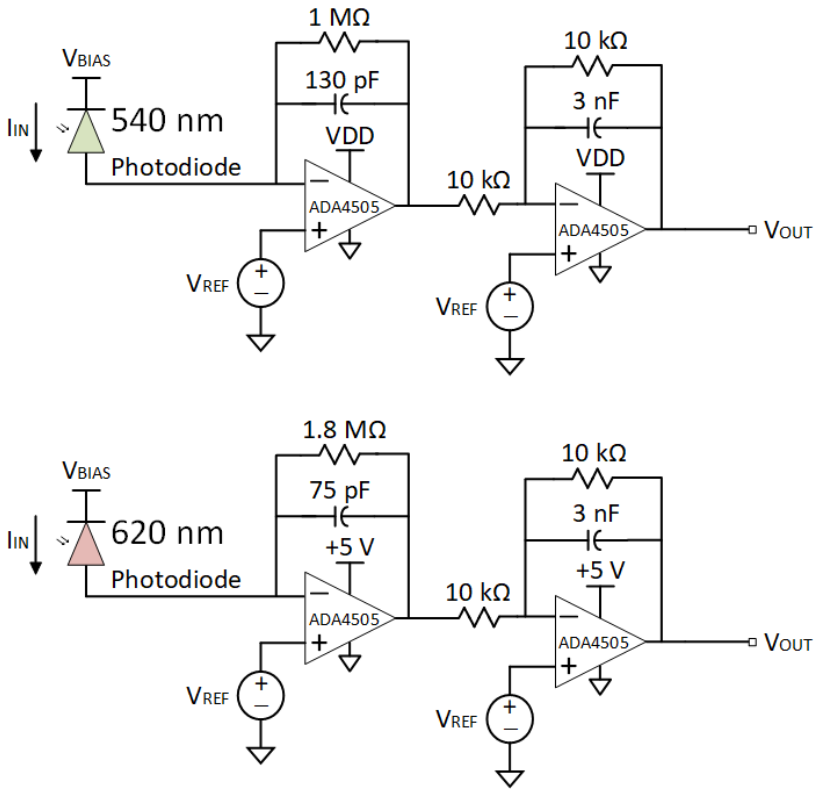

Figure 2.6: Schematic of optical recording block.

For the COTS opamp component, an ADA 4505-2 was selected for the following reasons:

- Low opamp current noise spectral density of 20 fA/$\sqrt{Hz}$
- Low voltage noise spectral density of 65 nV/$\sqrt{Hz}$
- Gain-bandwidth product of 50 kHz
- Quiescent current consumption of 172 μA

For the 520 nm and 620 nm photodiodes, a Vishay TEMD6200 and Osram SFH2716 were selected respectively. The main driver for this selection was the value of the junction capacitance (C_J) and shunt resistance (R_{SH}), representative of the parasitic capacitance and resistance across the PN junction. C_J in particular is of importance because it acts as the input capacitance to the TIA and can limit the circuit bandwidth. Therefore, a smaller C_J is desirable. The C_J and R_{SH} values for the 520 nm photodiode with no reverse bias are 60

pF and 2 GΩ. For the 620 nm photodiode under the same bias conditions, the values are 28 pF and 1 GΩ.

2.4.2 Stability Analysis

One of the challenges of TIA design is ensuring stable AC and transient operation. The following three analyses can be run to verify stability:

(i) Open-loop gain and $1/\beta$ plot to ensure the roll-off is -20 dB/dec before and after the point-of-intersection [24]

(ii) Input small-signal square waves to observe any overshoot or ringing

(iii) Parasitic capacitance sweep in feedback to see the effect on bandwidth

For the first analysis, to plot both the open-loop and feedback gain simultaneously the feedback loop must be broken at the input and the negative terminal of the opamp should be connected to a LC feedback circuit.

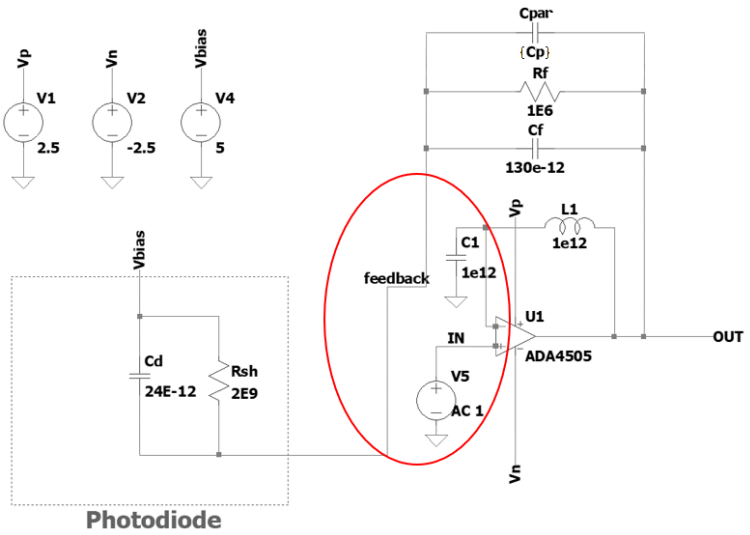

Figure 2.7: Schematic of testbench for isolating phase-shift of opamp and feedback circuits.

This LC circuit sets the DC bias of the transistor by using large inductance and capacitance values that produce a very low-frequency pole. Then, an AC voltage source can be used

at the input of the positive opamp terminal. The feedback gain is taken as $V_{feedback}/V_{out}$. The advantage of this analysis is the individual phase shift contribution of the open-loop circuit and the feedback circuit is visible. As can be seen in Figure 2.8 with the red plot, R_f creates a first-order zero that causes the feedback circuit response to increase at 20 dB/dec. Similarly, the open-loop plot presents a first-order pole response with a slope of -20 dB/dec. The intersection of these lines at frequency f_{int} adds a 180° phase shift at the output which is already 180° phase-shifted by the natural inversion of single-stage opamp circuit. As a result, at f_{int} the circuit will be unstable. Since a pole must exist in open-loop response to define the bandwidth, the only way to limit the phase shift is to create a pole to cancel out the zero in the feedback loop. As can be seen with the blue plot, the addition of C_f compensates the feedback response and ensures circuit stability.

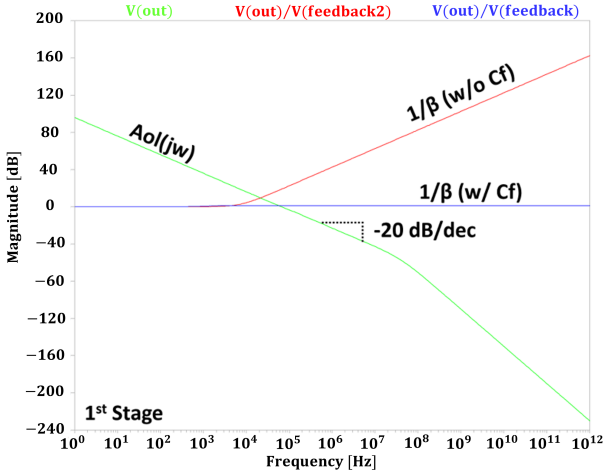

Figure 2.8: First-stage TIA open-loop response and feedback response with and without the feedback capacitor.

While feedback analysis is a good predictors of circuit stability, it is always prudent to perform transient analysis simulations to identify any peaking or ringing behavior. In addition, system delay between output and input can only be determined with this method. Transient analysis is performed by inputting a small amplitude square wave at the input. A square wave contains both high and low-frequency components, therefore it thoroughly tests stability across a range of frequencies. For the purposes of the designed system, a 10 nA

current square wave was fed into the input.

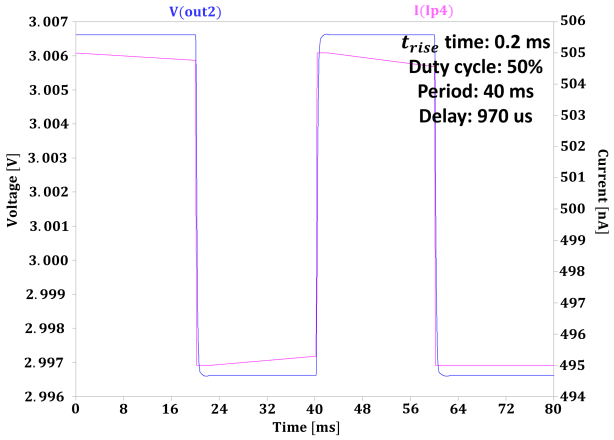

Figure 2.9: Cascaded two-stage TIA transient square wave input.

Finally, to account for parasitic shunt capacitance (C_{par}) coming from the feedback resistor, the C_{par} was swept from 1 pF to 100 pF to observe the effect on bandwidth. As can be seen in Figure 2.10, even for a large parasitic capacitance of 100 pF the bandwidth is still acceptable for the application signal characteristics.

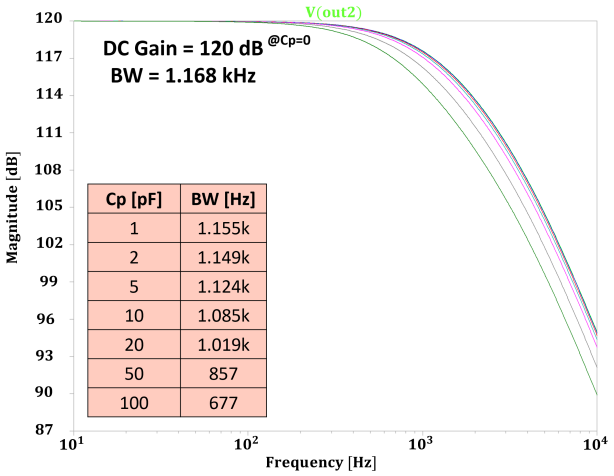

Figure 2.10: Cascaded two-stage TIA parasitic capacitance sweep.

Similar stability analysis was done for each individual stage of the TIA. These plots can be found in Appendix A.

2.4.3 Noise Analysis

Due to the low-frequency, low-amplitude nature of the signal-of-interest, $1/f$ and thermal noise sources are important to analyze. For a TIA, the amplifier voltage noise (e_n), current noise (i_n), the thermal noise generated by feedback resistor ((e_n)), and the dark current noise ((i_d) from the photodiode are the primary contributors to overall noise. The amplifier noise sources are represented in Figure 2.11.

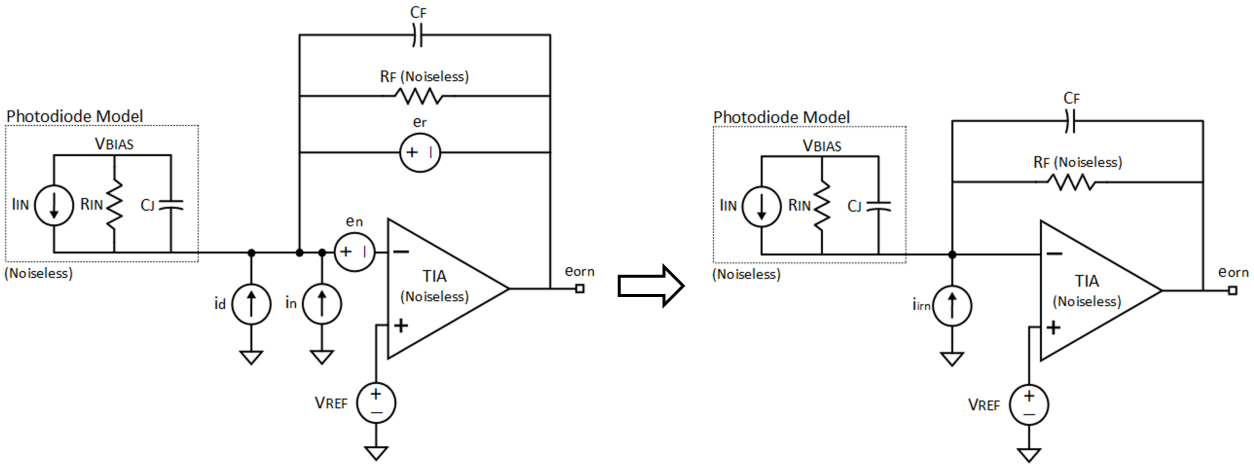

Figure 2.11: TIA simplified model with voltage and current input-referred noise sources.

These noise sources can be combined into a single input-referred current source. The bandwidth-extending effect of the input capacitance is also accounted for in Equation 2.6 [25]. The overall input-referred current noise (I_{irn}) is the squared sum of the RMS voltages divided by the TIA mid-band gain (BW). To plot the I_{irn} spectral density over frequency, the Analog Devices LTSpice simulation software was used.

$$I_{irn} = \sqrt{{i_n}^2 + \frac{{e_n}^2}{R_F} + \frac{4kT}{R_F} + \frac{e_n \cdot 2\pi \cdot BW \cdot {C_J}^2}{3} + 2qI_D \cdot BW} \tag{2.6}$$

As can be seen in Figure 2.12, the I_{irn} is dominated by $1/f$ noise. The output-referred voltage noise V_{orn} follows a similar profile at lower frequencies. However, around 1 kHz V_{orn} behavior starts to diverge as the amplifier gain limits the voltage noise bandwidth. The RMS noise at at a given frequency can be approximated from the plot by identifying the

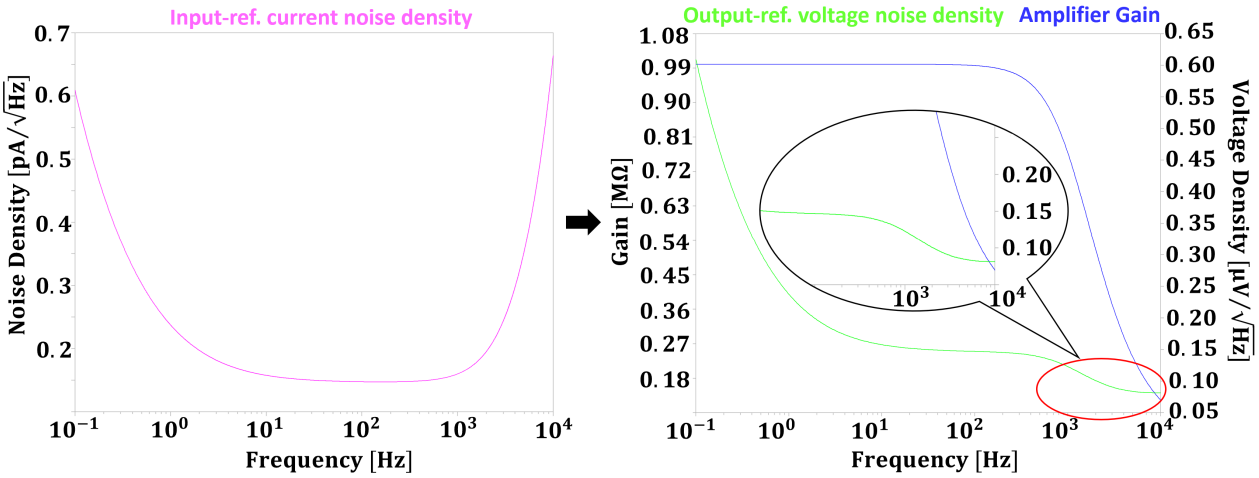

Figure 2.12: Input-referred current noise, amplifier gain, and output-referred voltage noise.

noise spectral density and multiplying by the square root of bandwidth. Therefore, for a bandwidth of 1 kHz the output voltage noise of the system would be 1.3 .

2.4.4 TIA Measurements

As a first step prior to testing the analog front end (AFE), characterization of the TIA was carried out. Since TIA designs are sensitive to input capacitance, using a current probe at the input to measure photocurrent is not viable. Therefore, a three-step process can be employed where the IV curve of the photodiode is first determined after which the TIA voltage gain is recorded. Using the IV characterization curve, the voltage gain can then be converted to transimpedance gain.

Lab measurements with this technique are shown in Figure 2.13. The photodiode IV curve was obtained by setting a through-hole LED and the photodiode parallel to each other such that the light emitted from the LED was incident to the photodiode. The DC voltage across the LED was then swept from 0 V to 5 V and the resulting photodiode current was measured with an ammeter. The forward voltages given in the plot represent the voltage across the LED that produces the minimum illuminance the photodiode can detect. For the gain curves, a sine wave voltage signal was used to drive the through-hole LED. The frequency of this signal was swept from 1 Hz to 10 kHz. The amplitude of the input current signal was

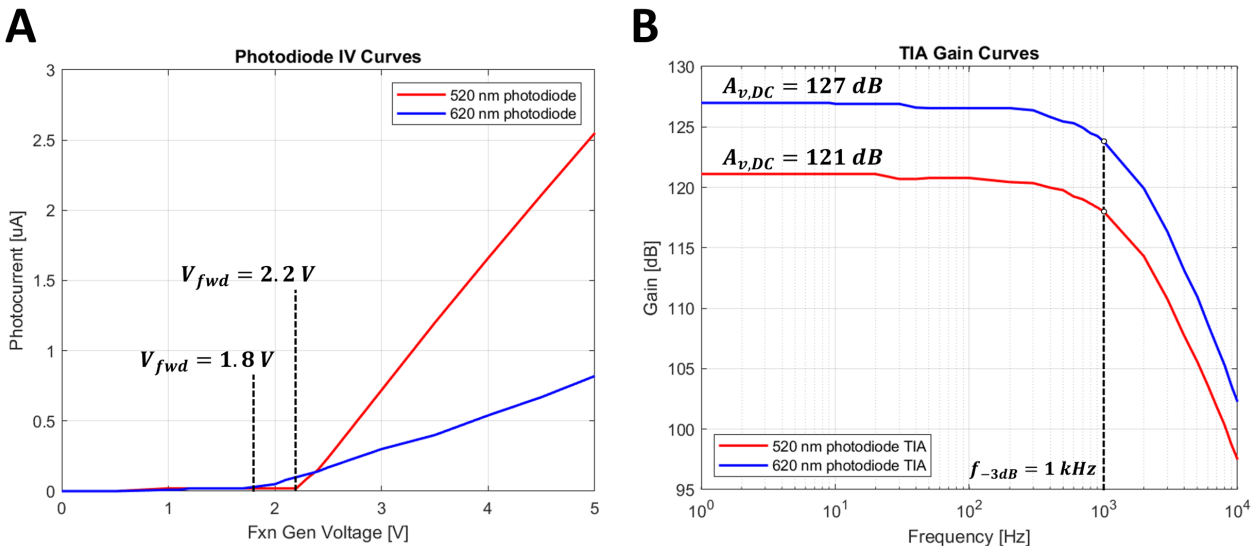

Figure 2.13: (A) Photodiode IV curves. (B) TIA gain bode plots.

determined by using the photodiode IV curve and correlating the voltage amplitude to the resulting photocurrent.

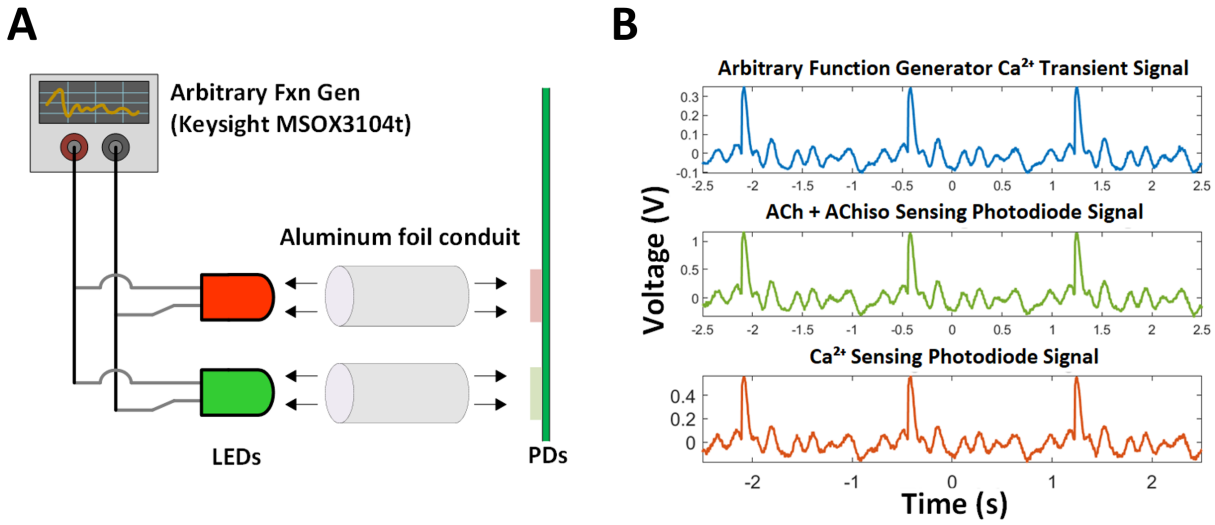

Figure 2.14: (A) Illustration of testing procedure for TIA block. (B) Arbitrary function generator Ca^{2+} transient signal and measured PD signals.

Following TIA characterization, an in-vivo test methodology was devised. In this methodology, through-hole LEDs were driven with brain data emissions recorded with a fiber photometry device. This data was recorded from live animal experiments carried out by our collaborator from Kanazawa University [26]. The light from these LEDs was directed to-

wards the on-board photodiodes through a reflective aluminum foil conduit to increase light intensity and reduce interference. Both the testing procedure and recorded signals are presented in Figure 2.14. As can be seen in Figure 2.14(b), the brain data signals fed into the input are replicated at the output demonstrating the AFE measurement ability.

2.5 Board Layout

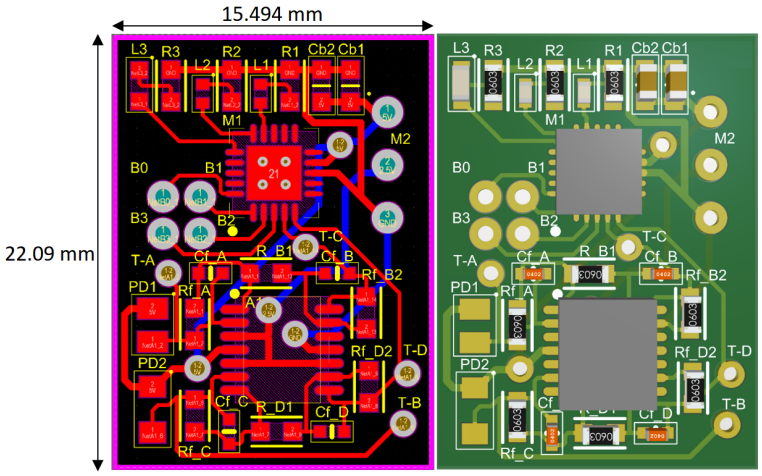

Figure 2.15: PCB layout.

The PCB layout used for this design is shown in Figure 2.15. The board is composed of two layers and uses two voltage sources. The 5 V source is to power the MCU and the opamp. The 2.5 V source is used to provide a common-mode DC bias to the opamp's positive input terminal. All voltages are supplied through the voltage supply header and are routed through the top and bottom layers. A total of four test points are provided. These test points are placed at the input and output of each TIA block. To make the device wireless, a coin cell battery was placed on the back of the board.

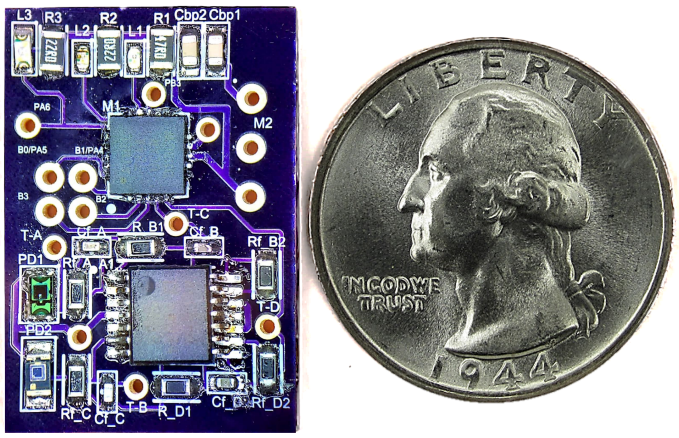

Figure 2.16: Populated board micrograph.

2.6 Prototype Limitations

Despite this prototype meeting all the design goals listed at the beginning of this section, there were some inherent limitations with this device. One such limitation was the lack of wireless power transfer (WPT). Even though a battery was used to make the device untethered, the coin cell adds weight to the device and holds charge for a finite period of time dependent on the stimulation and measurement period. In contrast, using an antenna to wirelessly power the device allows for unlimited device life as long as the antenna is within range of the external transmitting power source. Another related limitation of this prototype was the lack of wireless data transmission. In the current system, data is stored on the limited memory of the MCU and periodically downloaded to an external computer when the battery is being replaced. With an antenna added to address the lack of WPT, wireless data telemetry can also be implemented through low-power backscatter communication.

Another issue with this device was the decision to go with a COTS design. This design choice was made to ensure fast and reliable measurement results that would allow us to become familiar with the application and signal characteristics in this application. However, the tradeoff was higher power consumption. This limitation can be rectified with an integrated circuit solution as presented in the next section.

Chapter 3

Photometry Device: Integrated Circuit Prototype

3.1 Design Goals

The purpose of second prototype was to address the drawbacks of the first prototype and provide additional results to support the Human Frontiers Grant proposal. To do this, it was decided that the second prototype would be both a product and evaluation board used to characterize an optical stimulation and recording chip designed and taped out by two PhD students in our lab, Ian Costanzo and Devdip Sen, for another application. By measuring a chip, the technical drawbacks of the design could be identified and avoided for the subsequent tapeout planned for the coming third iteration of the device. The design criteria for this device retained the first two features from the first prototype comprising of simultaneous driving of LEDs and measurement of emissions. Adding to these were the following criteria:

(i) Tapeout IC-design for LED stimulation and optical front-end

(ii) Wireless power transfer (WPT)

(iii) Wireless data telemetry

3.2 Block Level System

As can be seen in Figure 3.1, the system is made up of two chips taped out by ICAS lab PhD students (hereon referred to as "Tapeouts"). The system consists of a power management block which includes a low dropout regulator (LDO) and a bandgap reference (BGR) to produce the voltage biases used to appropriately bias other portions of the chip. The other two blocks are an LED driver and an analog front-end that optically stimulate neurons and record the emissions. These blocks are duplicated in a second channel within Tapeout 1. The only difference between the channels is in the LED driver block where the second channel contains an external power transistor to select the LED that must be stimulated, as shown in Figure 3.1. This was necessitated by the fact that Tapeout 1 only had two LED drivers while there are three LEDs that need to be stimulated.

To enable WPT, an antenna was included. The antenna output can be rectified through the active rectifier present on Tapeout 2 or through a COTS rectifier placed on the board. An external LDO is also included to provide the supply to Tapeout 1. The input to the LDO can be taken from any of the two rectifier outputs or from an external battery source. In addition, for characterization of the Tapeout 2 active rectifier, a Sub-Miniature Version A (SMA) connector is included at the rectifier input.

The final major component on the board is an ATTiny84 MCU. The internal MCU ADC is used to digitize the AFE output signal. The MCU also provides the driving signal for both the LED driver as well as the NMOS switch that enables backscatter communication.

3.3 Wireless Power Transfer and Data Telemetry Block

3.3.1 System Design

In the previous iteration of the prototype, a battery was used to make the device untethered. However, the need to repeatedly charge the battery limited the length of experiments.

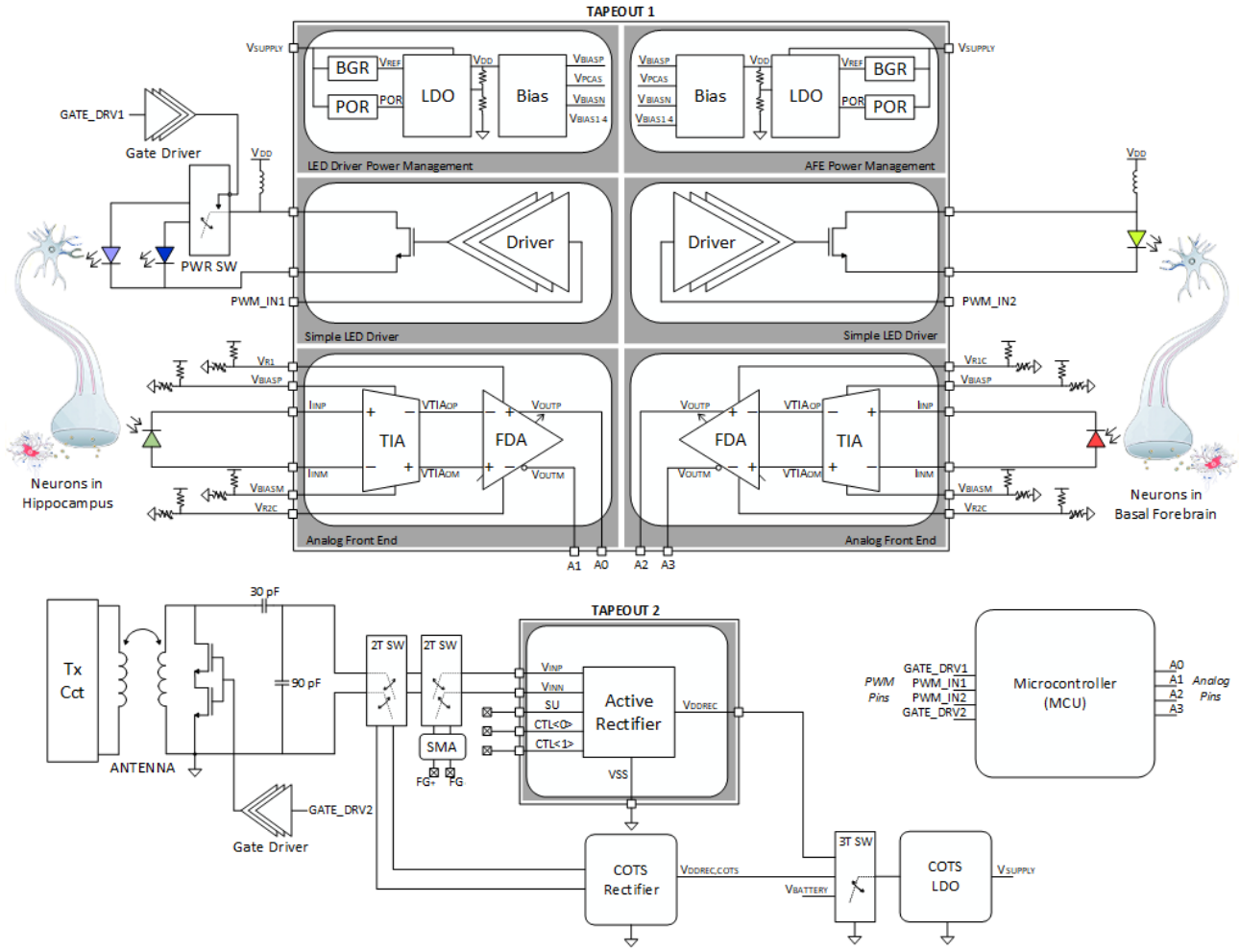

Figure 3.1: High-level illustration of system.

To do away with this limitation, this prototype was equipped with WPT capabilities. To provide wireless power, a planar antenna was designed to operate with Radio-Frequency Identification (RFID) protocol at 13.56 MHz. The antenna was designed in the Altium PCB Designer tool and exported to Ansys HFSS, a three-dimensional field solver software. The scattering matrix parameters were extracted through simulation and used to import the antenna into an Advanced Design Systems (ADS) schematic. In ADS, a matching network was generated to match the receiver antenna input impedance to the complex conjugate of the COTS rectifier input impedance. To transmit power to the board, a power amplifier circuit was designed on a separate board.

In addition to wireless power, a truly untethered device can also send data without having

to be plugged in. This is a hard requirement to meet because wireless data telemetry generally consumes a lot of power, more than can be provided by a WPT circuit. Therefore, to send data in a low power manner, a backscatter communication technique was chosen. With this technique, a data signal is superimposed on the power transfer signal by modulating the receiver power such that the coupled transmitter circuit signal also modulates. In this board, this was achieved by connecting two power NMOS transistors in series at the input of the receiver antenna. The microcontroller provided the PWM signal that turns on and off the NMOS switch through a gate driver. When the switch is on, the inputs of the receiver antenna are shorted together to ground and this momentary 0 V point is observed at the transmitter antenna. Therefore, by modulating the shorting of the receiver antenna input, a binary data stream can be sent back at low-frequencies to the transmitter board. This modulation scheme is referred to as On-Off Keying (OOK).

3.3.2 WPT and Data Telemetry Lab Measurements

To test the WPT circuit functionality, the transmitter board was driven with a 13.56 MHz square wave. The transmitter and receiver boards were placed together and the coupled signal was observed.

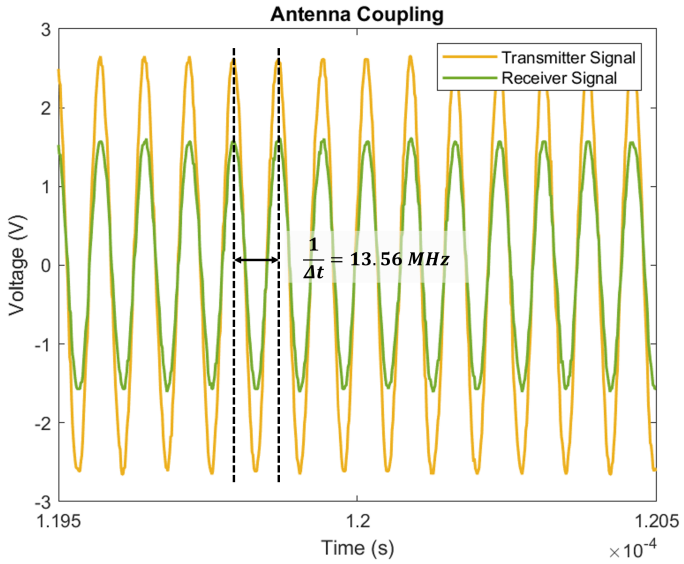

Figure 3.2: Plot of antenna signals at the transmitter and receiver board.

This signal was then fed into the input of the COTS rectifier. At the output of the rectifier, a 1 uF capacitor was added to minimize the ripples at steady-state operation and store charge to maintain the output voltage.

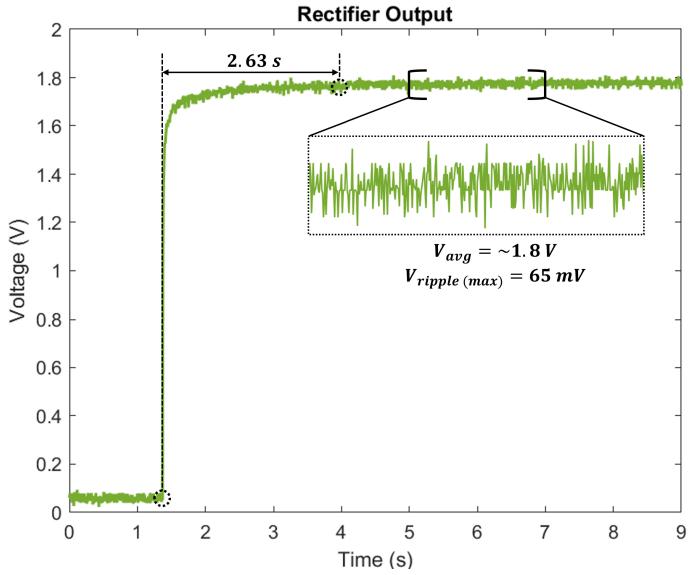

Figure 3.3: Plot of rectifier output.

To test the data telemetry circuit, a 3.3 V square wave was generated by the MCU and fed to the gate of the power MOSFET. After testing, it was found that the 3.3 V signal was not strong enough to effectively turn on and off the MOSFET switch. Therefore, to provide enough power sourcing capability a TC426 gate driver with a 1.5 A maximum source current was used. This amount of current far exceeds the required current needed to pull the gate of the MOSFET down. In a future iteration of this device, a COTS gate driver with an appropriate current sourcing specification will be used. In addition, a 3.3 V boost converter will be added to produce the necessary driving signal amplitude on-board without any external inputs. The driving signal frequency was progressively increased to identify the highest frequency of operation. With backscatter communication, up to 1 MHz data speed was achieved. Assuming a bandwidth of 100 Hz based on the spectral frequency plot given in Figure 2.5, the required data transfer rate can be calculated as x10 of this value which comes out to 1 kHz. This shows that the backscatter communication is more than capable

of transferring the output data without compromising resolution. The one issue that was seen was the approximately 500 mV ringing for the driving signal which was likely due to the parasitic inductance of the long ground clip of the scope probe. Using a pigtail scope ground would reduce the wire length and attenuate the ringing.

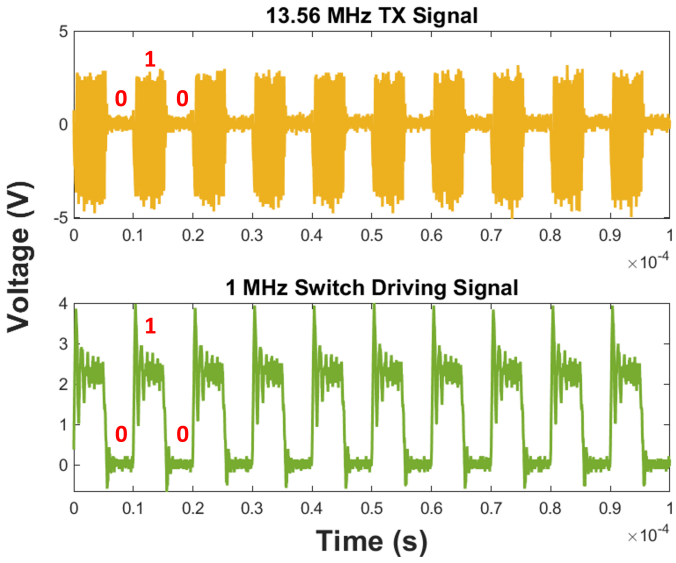

Figure 3.4: Plot of MOSFET switch driving signal and resulting receiver signal with the overlaid backscatter data.

3.4 On-chip Power Management Block

3.4.1 System Design

In this block, four power management blocks were included each consisting of an LDO, a beta multiplier reference (BMR), and a bias generator. This design decision was made to ensure that each LED drivers and AFE had its own dedicated LDO circuitry.

Diving into the circuit details, a simple LDO topology consisting of an operational transconductance amplifier (OTA) with negative feedback was implemented. In this circuit, the feedback voltage divider ratio determines the regulated voltage value. At the output, a NMOS source follower isolated the load thereby maintaining the amplifier gain which needs to remain high. Compared to a traditional opamp which has a dominant pole internal to the

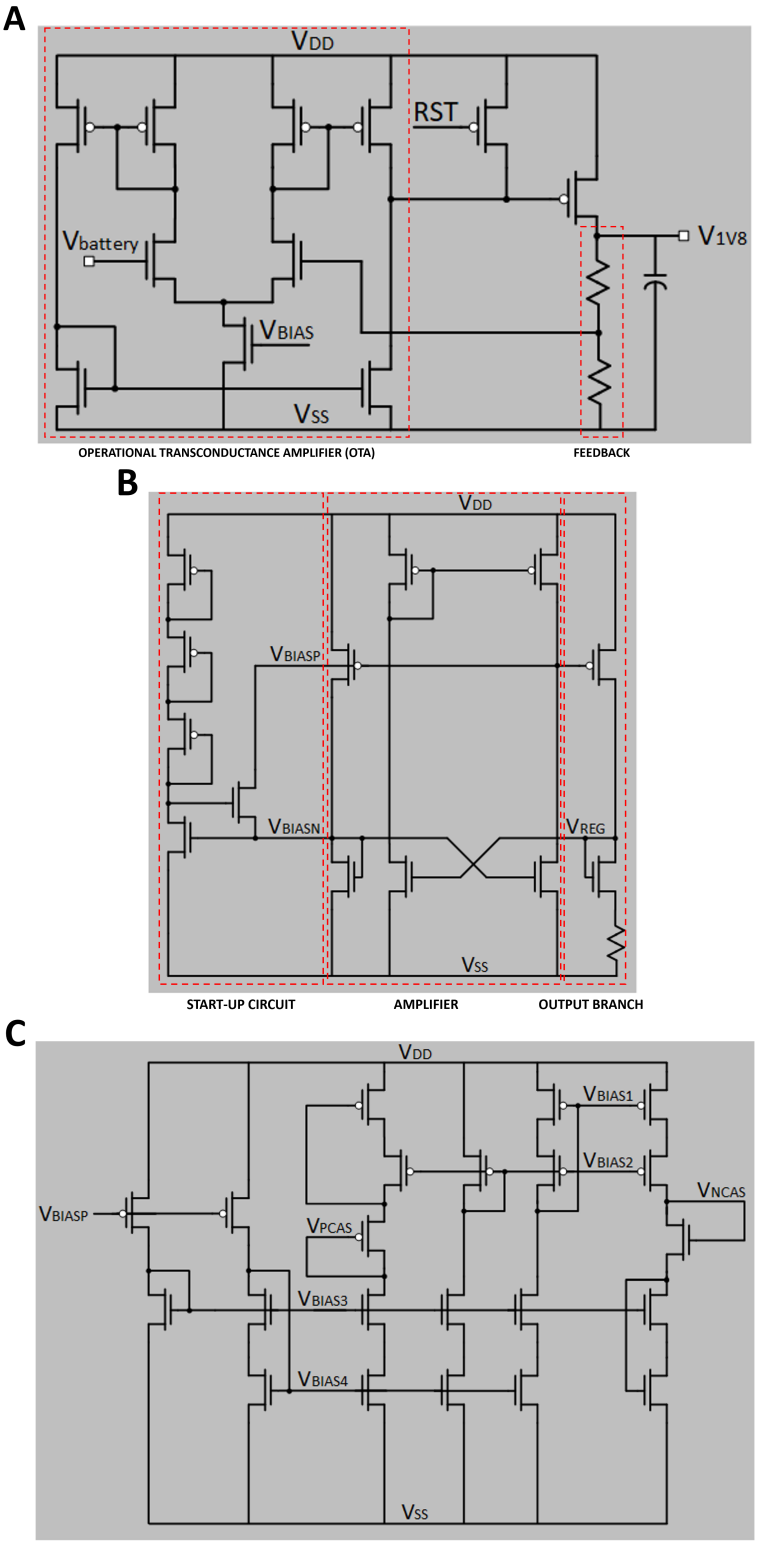

Figure 3.5: Schematic of (A) LDO topology, (B) BMR topology, and (C) Bias Generator topology.

first stage, an OTA was used as the error amplifier in this case because it has no first-stage dominant pole which improves stability. In addition, a large capacitor was placed at the load to dampen out peaking which can trigger oscillations.

In addition to generating a 1.8 V supply voltage, twelve other smaller voltages were generated to bias other blocks on the chip. To create these voltages, a BMR and a short-channel biasing circuit were utilized. These designs are based on circuits presented in [27]. The basic operating principle of the BMR topology is to create a difference in gate-source voltage (V_{GS}) between two NMOS transistors by including a reference resistor that degenerates the source.

The voltage drop across the resistor created by this difference in V_{GS} conducts a current that can be controlled by the size of the output branch transistor or the resistor value. An amplifier is included in the design to equalize the drains of the two NMOS transistors and, as a result, decrease sensitivity to supply variations. The Vbiasp voltage from the BMR is fed into the biasing circuit which in turn produces voltages that can be used to bias different circuits. The circuits discussed are shown in Figure 3.5.

3.4.2 Power Blocks Post-Layout Simulations

To verify the operation of this circuit prior to taping out the chip, post-layout simulations were carried out. In the testbench, a 3.3 V signal was supplied to the LDO input. To mimic a testbench supply, the voltage was slowly ramped to the final voltage instead of being initialized at 3.3 V. The voltages for each node after stabilizing are shown on the left of Figure 3.6.

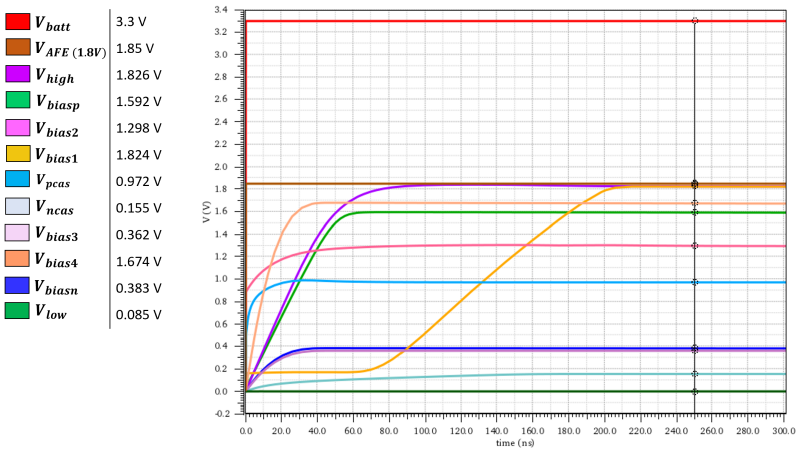

Figure 3.6: Simulation plot of bias voltages at the output of the BMR and BGR blocks.

3.4.3 Power Blocks Lab Measurements

In lab, a similar testbench to the one used in simulation was setup. A standard DC supply was used to supply a 3.3 V signal. The voltages measured in lab were comparable to those found in simulation.

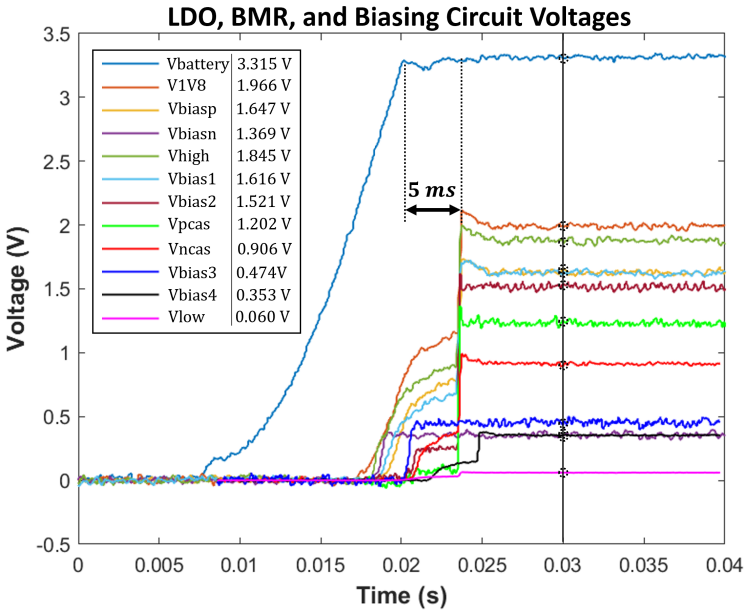

Figure 3.7: Lab measurements of bias voltages at the output of the BMR and BGR blocks.

In addition to checking the bias voltages, line and load regulation plots were also acquired. The line regulation plot was measured by ramping the input voltage and observing the output. Similarly, the load regulation plot was measured by setting the input voltage to a constant

3.3 V and sweeping the load with progressively smaller resistors. The plots in Figure 3.8 show that the LDO remains stable over a large range of input voltages and loads.

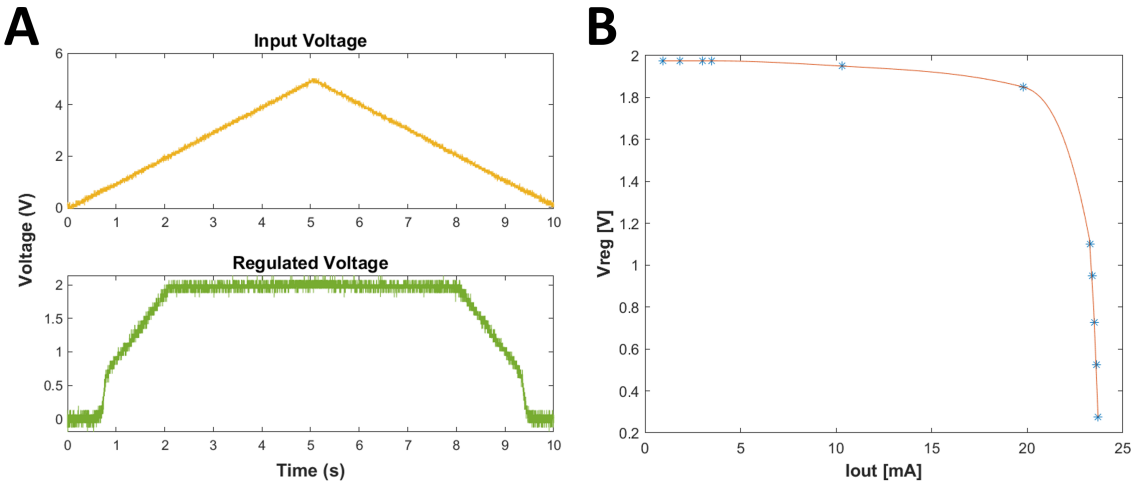

Figure 3.8: Lab measurements of (A) LDO line regulation, (B) LDO load regulation .

3.5 Optical Stimulation Block

3.5.1 System Design

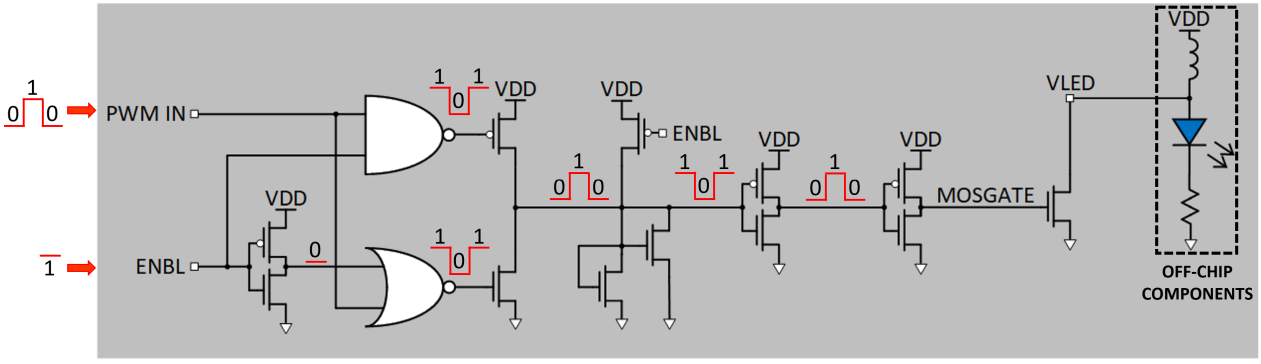

Figure 3.9: Schematic of the LED driver topology including external components.

The LED driver topology used in Tapeout 1 is shown in Figure 3.9. A PWM signal is provided by an on-board MCU at the input of the LED driver. A NAND-NOR stage either inverts or passes the input dependent on the enable signal value. From there, three inverters increase the PWM signal drive strength and feed it to the gate of a large power

NMOS transistor at the output. At the drain of this transistor, an external LED is connected to ground through a current-limiting resistor. An external inductor is added in series with the LED to complete the boost converter-inspired topology. When the LED drive signal is high (i.e. 1), transistor M0 turns on and provides a low-resistance path to ground that builds up the magnetic field around the inductor. When the drive signal is low (i.e. 0), transistor M0 turns off and the built-up inductor current is dumped to the LED input node boosting the voltage above the rated forward voltage. As a result, the LED conducts current which is modulated by the PWM signal controlling the switching frequency of power NMOS transistor. To decrease the amplitude of the current pulse, the ON period of the PWM signal can be decreased. With a shorter period to charge the inductor, the V_{LED} node voltage is boosted to a lower value which will result in less LED current conduction. Similarly, the PWM ON duty cycle can be made longer to generate higher amplitude LED currents.

To turn off the LED driver, an PMOS enable switch (transistor M17) is included after NAND-NOR stage. When this switch is high, the transistor is 'off' and input signal passes to the inverter stage. If the enable signal is low, the transistor turns 'on' and pulls the node to ground through transistor M16.

3.5.2 LED Driver Post-Layout Simulation

Post-layout simulations were carried out to test circuit operation. A 20% duty cycle, 40 Hz square wave was fed to the input of the driver to mimic the MCU-generated PWM signal.

The plots demonstrate the supply-boosting capabilities of the inductor. When the signal driving the NMOS transistor gate (G_{NMOS}) is high, the transistor is 'on' and voltage across the LED remains at ∼0 V. When the transistor shuts 'off', the LED voltage jumps up to 5.2 V allowing current to flow through the LED. The current is set by the series resistor.

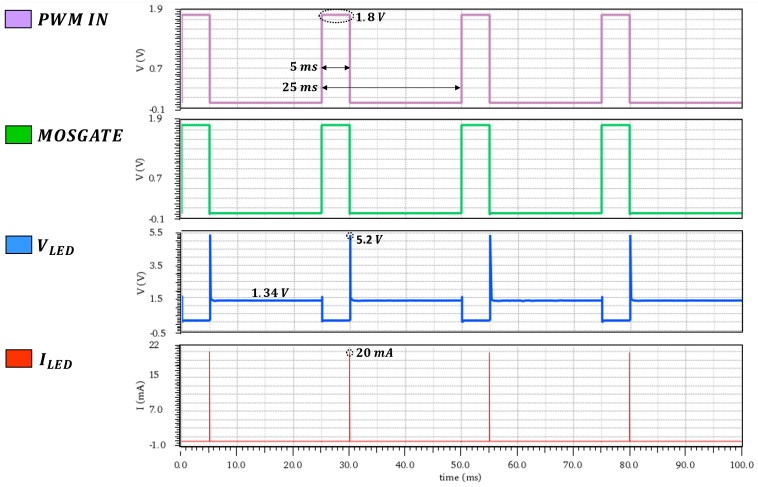

Figure 3.10: LED driver post-layout simulations.

3.5.3 LED Driver Lab Measurements

The simulation testbench was replicated in lab after the chip was received and wirebonded. The results are shown in Figure 3.11.

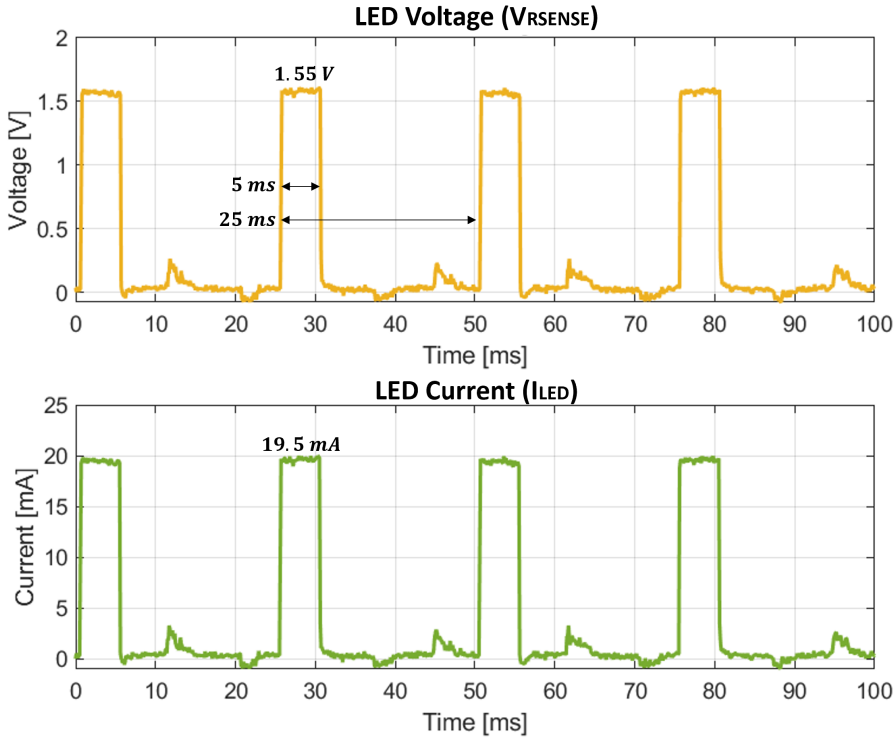

Figure 3.11: LED driver lab measurements.

3.6 Optical Recording Block

3.6.1 System Design

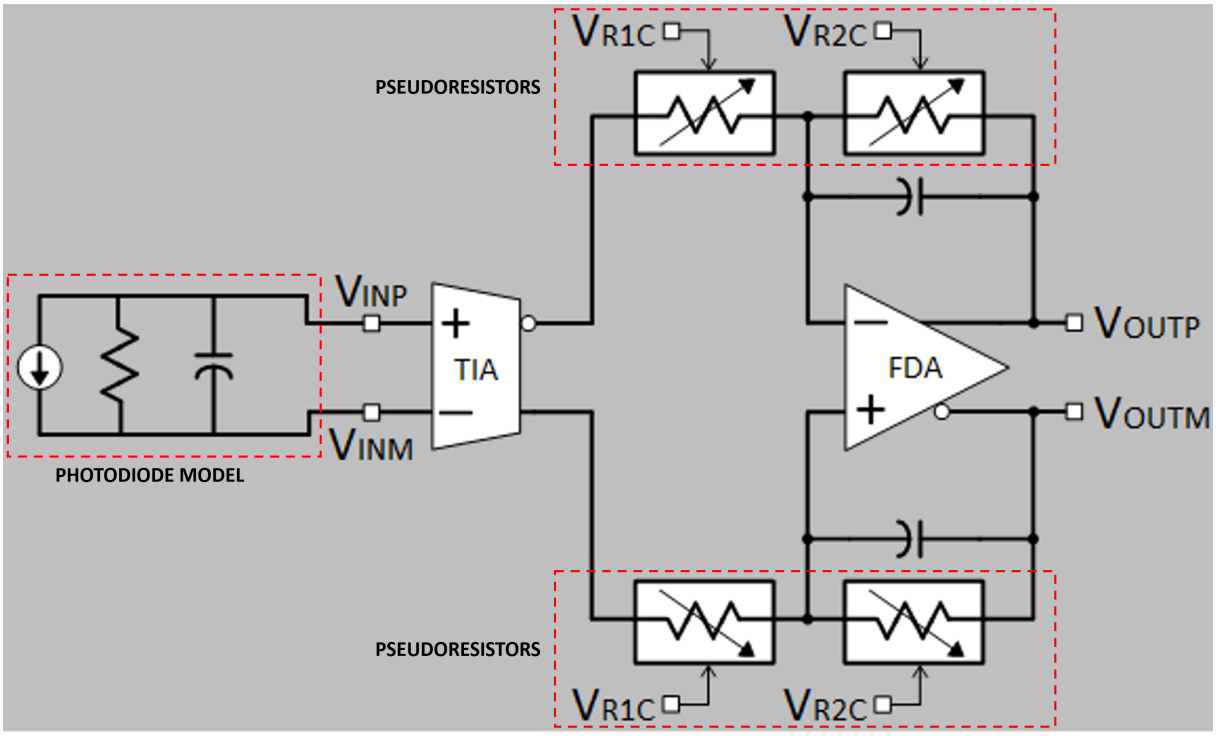

Figure 3.12: AFE topology schematic.

The AFE topology used in this block consists of a differential TIA followed by a variable gain fully differential amplifier (FDA). The gain of this topology is determined by the ratio of feedback resistor impedaces. is the assuming a large open-loop gain, we can approximate the overall AFE gain as follows:

$$A_{v(diff)} = \lim_{A_{OL}\to\infty} \frac{V_{out+} - V_{out-}}{V_{in+} - V_{in-}} = \frac{R_f}{j\omega C_f R_f R_i + R_i} \tag{3.1}$$

where R_f and C_f are the feedback resistance and capacitance, R_i and C_i are the input resistance and capacitance respectively.

The time constant formed by the feedback resistor and capacitor sets the bandwidth.

3.6.2 Transimpedance Amplifier Topology

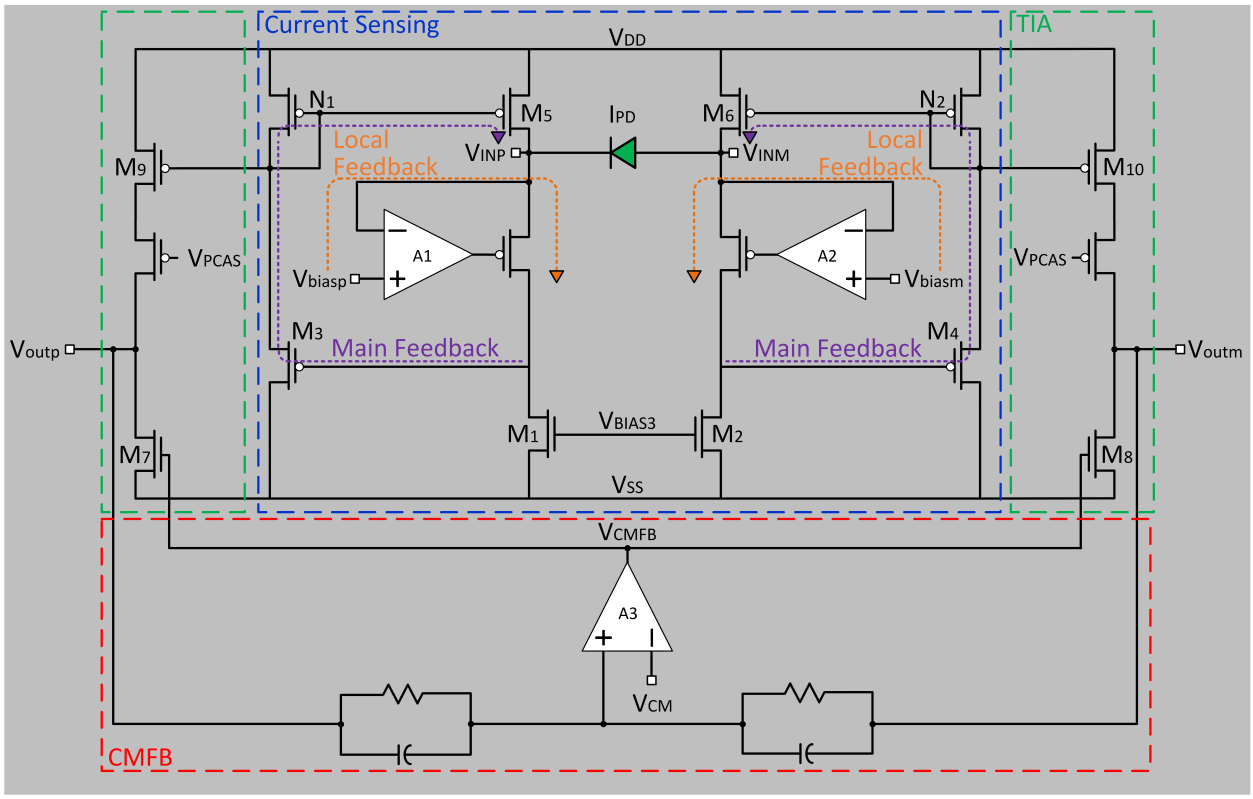

Figure 3.13: TIA topology schematic.

The TIA topology used in this chip was adopted from the circuit presented in [28], [29]. This topology can be broken down into three stages based on functionality. The current sensing stage sets the input DC bias level through a local opamp feedback circuit. The desired diode bias voltage (V_{biasp} and V_{biasm}) is supplied from an off-chip source. Due to the input equalizing capability of opamps A1 and A2, this voltage is mirrored to the TIA input. Using an external voltage allows for the positive and negative input of the diodes to be set to different voltages which will manifest in a bias across the photodiode. For applications where the photodiode must be reverse biased, this can be achieved by setting $V_{biasp} > V_{biasm}$. This TIA does not have a traditional negative feedback loop from input to output. Rather, the second stage of the current sensing circuit provides the main feedback mechanism. When the photocurrent increases, the current through the tail NMOS transistors (M1, M2) decreases and subsequently the gate of the second stage PMOS (M3, M4) stays low. This results in

more current being sourced by the second stage which pulls down nodes N1/N2. When node N1/N2 gets pulled down, this causes the first stage active load PMOS transistors (M5, M6) to source more current for the photodiode. The output branches act as the third stage of the current sensing circuit and provide the voltage outputs. Current from the photodiode branch is mirrored to the M3, M4 branch where the transconductance of the transistors M9, M10 convert the current into voltage. Lastly, the common-mode feedback (CMFB) stage works by averaging the inputs and comparing the result to the common-mode voltage. If either output goes up, the output of amplifier A3 will turn on the tail NMOS transistors (M7, M8) and pull the TIA output nodes down to the common-mode voltage.

3.6.3 Pseudoresistor Topology

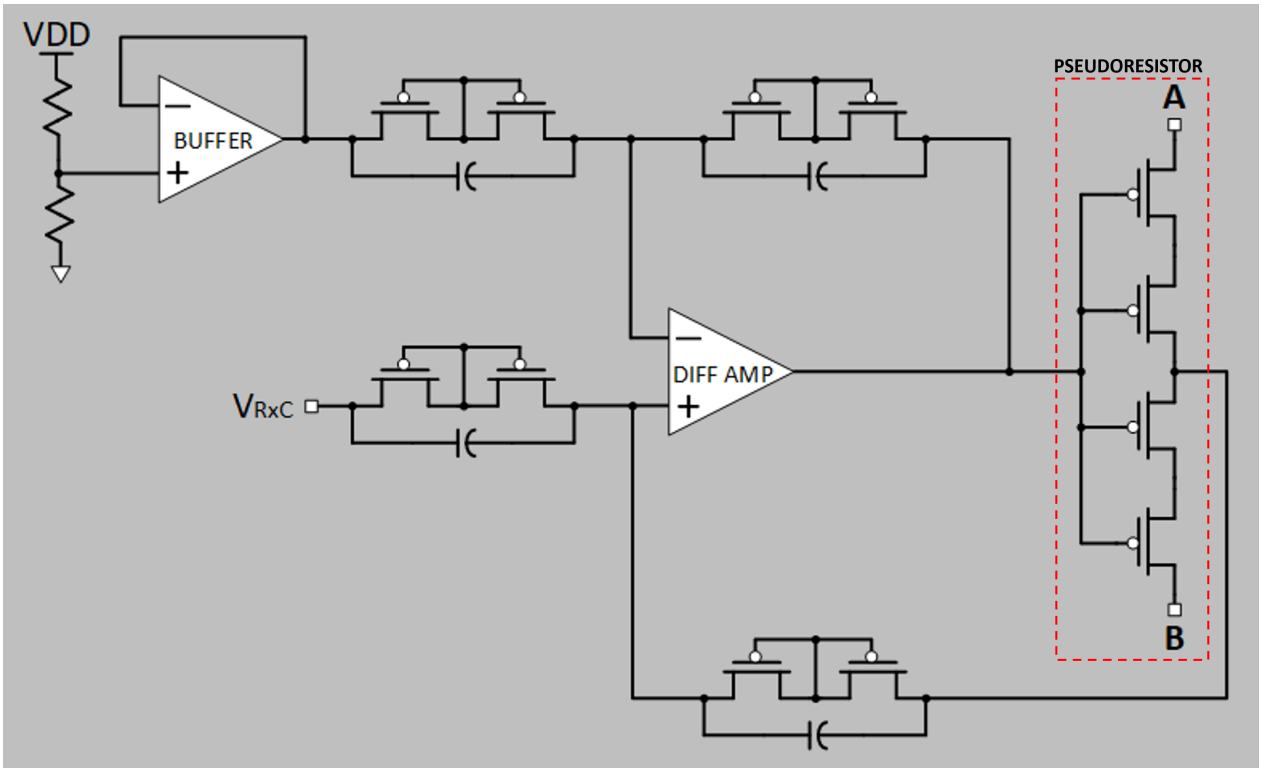

Figure 3.14: Pseudoresistor topology schematic.

To allow for flexibility in setting the gain and achieve low bandwidths, pseudoresistors were used in place of traditional resistors for input and feedback. The topology used was

based on a circuit presented in [30]. In this circuit, four PMOS transistors form the main pseudoresistor block. The gate voltage of these transistors is biased to the common-mode voltage (VDD/2) by a differential amplifier. The differential amplifier uses fixed-resistance PMOS pseudoresistors to achieve a high closed-loop gain. The voltage between terminal A and B is similarly set by the feedback loop and an external control voltage. The main purpose of the differential amplifier is to maintain the gate-drain voltage of the PMOS transistors at a constant value to ensure a linear change in resistance with respect to changes in the control voltage.

3.6.4 Fully Differential Amplifier Topology

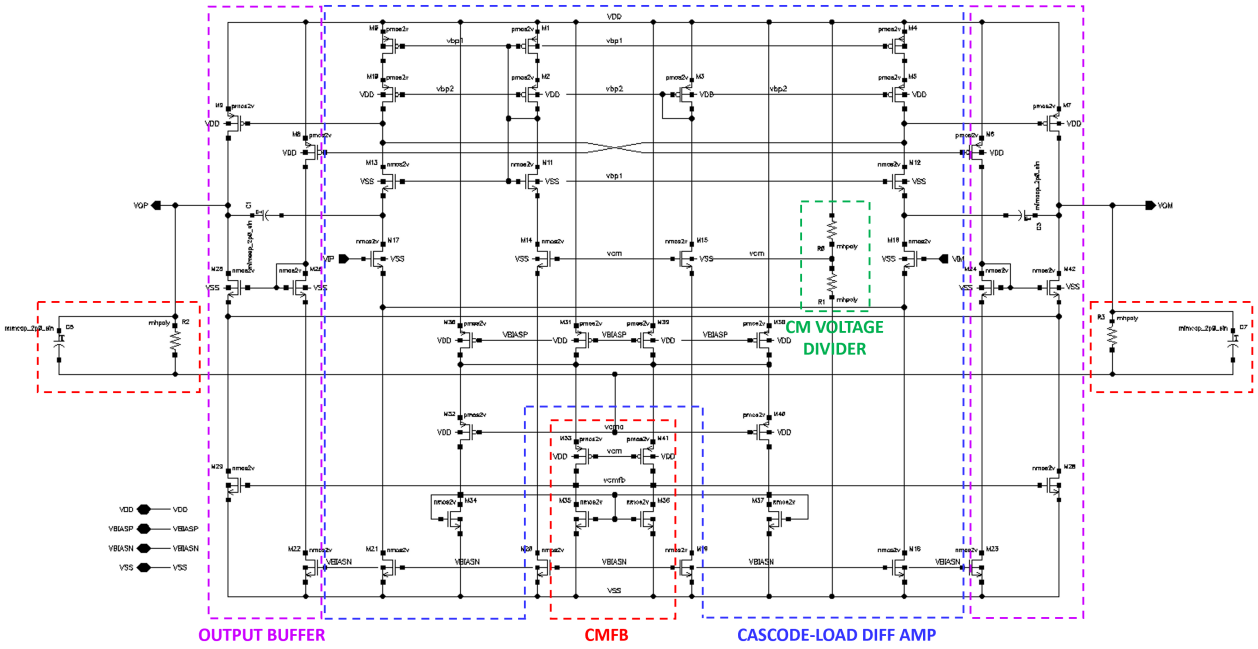

Figure 3.15: FDA topology schematic.

The FDA implemented in this chip was based of a circuit presented in [27]. Similar to the TIA circuit, this topology can be broken down into different sub-circuits. The main sub-circuit block is the cascode-loaded differential amplifier which is made up of a cascoded PMOS and NMOS input stage and a cascoded NMOS tail stage. Contrary to typical design where the tail stage is designed with two NMOS transistors, this circuit design reduces power

consumption by requiring only one bias voltage (V_{biasn}) to generate the tail current. Cross-coupled output buffers are added symmetrically to the design to prevent loading and increase capacitive driving capabilities. Finally, a CMFB circuit is included to maintain the output DC bias level. This circuit forms a negative feedback loop such that any difference between the output bias levels is amplified and fed to the gate of the output branch sink transistor. As a result, the transistor will compensate for the variation by sinking more or less current. This topology was chosen to match the symmetric nature of the previous stage TIA.

3.6.5 AFE Post-Layout Simulations

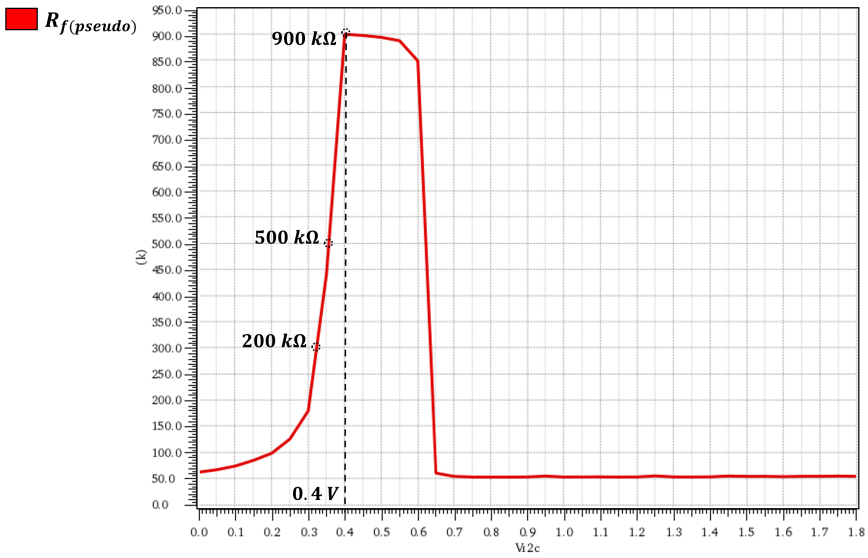

Figure 3.16: Pseudoresistor resistance when sweeping the R2 control voltage from 0 V to 1.8 V.

Several post-layout simulations were carried out to verify pseudoresistor operation, identify the optimal control voltage to maximize gain, and observe the AFE response to real input signals measured with a fiber photometry system. Starting with the pseudoresistor circuit, based on the recommendations given in [30] the transistors provide the most gain when the PMOS transistors are biased in subthreshold saturation. To identify the appropriate control voltage to achieve this transistor operating region, the control voltage was swept from 0 V to 1.8 V assuming a DC input current of 2 μA. This input current assumption was made

based on the average DC value observed when characterizing the photodiodes. As shown in Figure 3.16, the pseudoresistor value ranges from 50 kΩ to 900 kΩ. The highest resistance was achieved with a control voltage of 0.4 V.

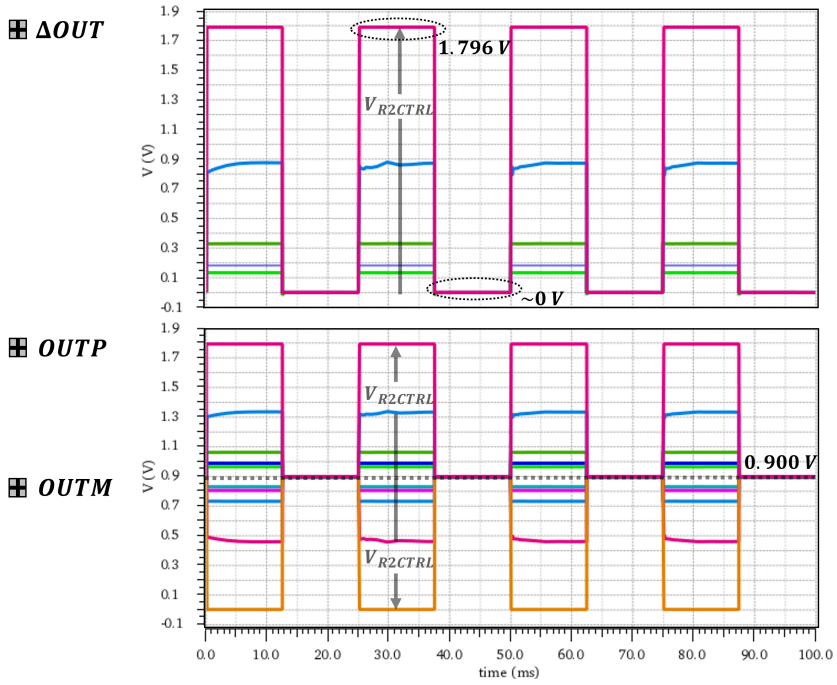

Figure 3.17: AFE independent and differential output voltage when sweeping the R2 control voltage from 0.1 V to 0.4 V.

To demonstrate the rail-to-rail operation of the AFE, a 40 Hz square wave with a 2 μA amplitude was fed into the input of the TIA. The individual outputs as well as the differential output plots for varying control voltage values is given in Figure 3.17. As predicted with the pseudoresistor simulations, the maximum gain was achieved at a resistor control voltage of 0.4 V.

Finally, to mimic realistic signal conditions, the fiber photometry brain data used for lab measurements with the first prototype was loaded into a piecewise-linear current source to test the AFE functionality under realistic signal conditions. The result is shown in Figure 3.18 where the input photocurrent is replicated at the output.

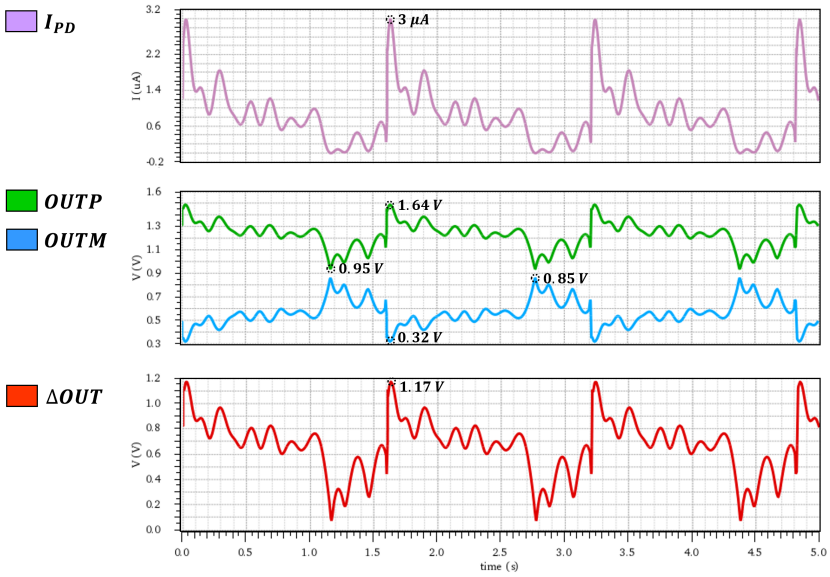

Figure 3.18: AFE transient simulation with a real photometry data fed to the input.

3.6.6 AFE Lab Measurements

To test the AFE circuit in lab, the same test bench shown in Figure 2.14(A) used for the first prototype, was utilized. After multiple cycles of testing, a differential measurement was not achieved. There were multiple reasons that made getting a differential measurement challenging. The main reason that can be cited was the short time frame given to learn and complete wirebonding of the chip. With no previous experience, a large portion of the time allocated for measurements was dedicated to learning how to properly wirebond. In addition, since this was the first tapeout produced by the ICAS lab, a double row of pads on the outer edge was used. In hindsight, this increased the complexity of wirebonding because it required the back row wires to be looped over the front row wires increasing likelihood of shorts. When it comes to debugging, the chip was pad-limited resulting in external access only available for the inputs and outputs. As a consequence, debugging issues with the chip without being able to probe important nodes such as the bias voltages was demanding. For these reasons, the chip results were inconsistent and all the input and output pads for any single AFE tested did not work as expected simultaneously.

Despite these issues, some of the chips did work partially. In one chip, the INM to OUTM

signal chain functioned as expected, and in another AFE on the same chip the INP to OUTP signal chain behaved consistently as well. Therefore, to extract results from the AFE, a single-ended excitation was applied to each of these independent AFEs as shown in Figure 3.19. For the negative input excitation, the photodiode was used in photovoltaic mode (i.e. with no reverse bias). For the positive input excitation, a reverse bias was applied to the photodiode to increase the amplitude of the input photocurrent signal. If the measurement were to be repeated, the pseudoresistor control voltages would have been changed to increase the AFE gain rather than reverse bias the photodiode. The results of the single-ended excitation are shown in Figure 3.20.

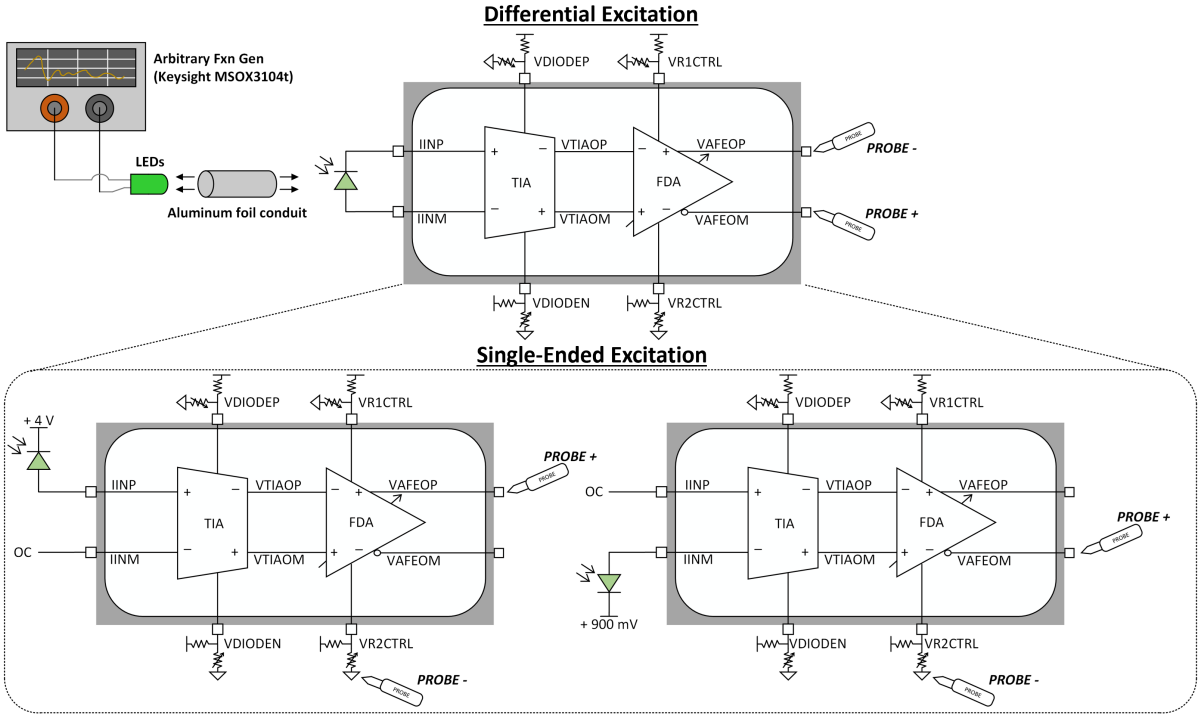

Figure 3.19: Comparison between differential and single-ended excitation.

The single-ended excitation does replicate the input photocurrent. However, there is a clear amplitude cutoff that indicates that the through-hole LED used to mimic the neuron emissions does not turn on below ∼2.5 V resulting in no signal below this voltage. With the pseudoresistor control voltage values of VR1C = 0 V, VR1C = 0.75 V used in this measurement, a single-ended gain measurement was made. The single-ended gain is about

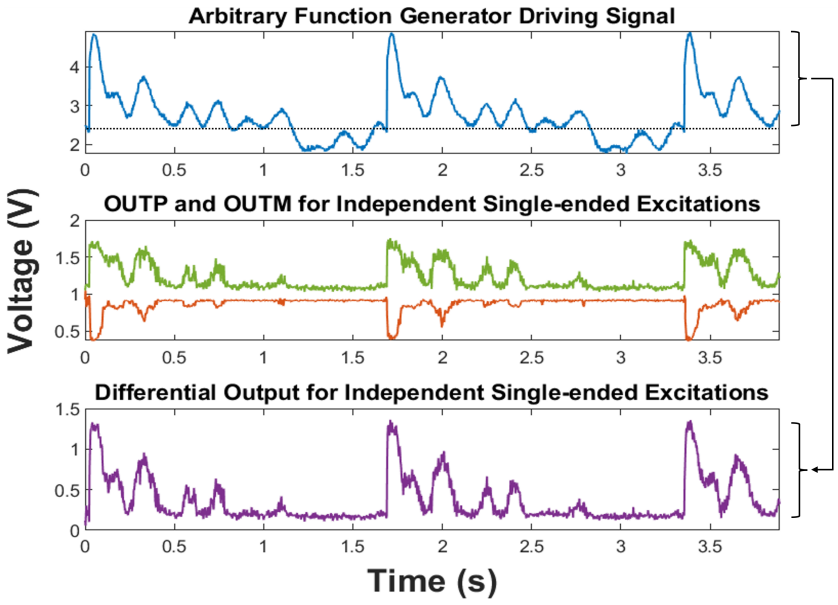

Figure 3.20: AFE outputs from single-ended excitation measurements.

10 dB less than the gain produced by the first prototype which is consistent with the observed amplitude cutoff for the input photocurrent.

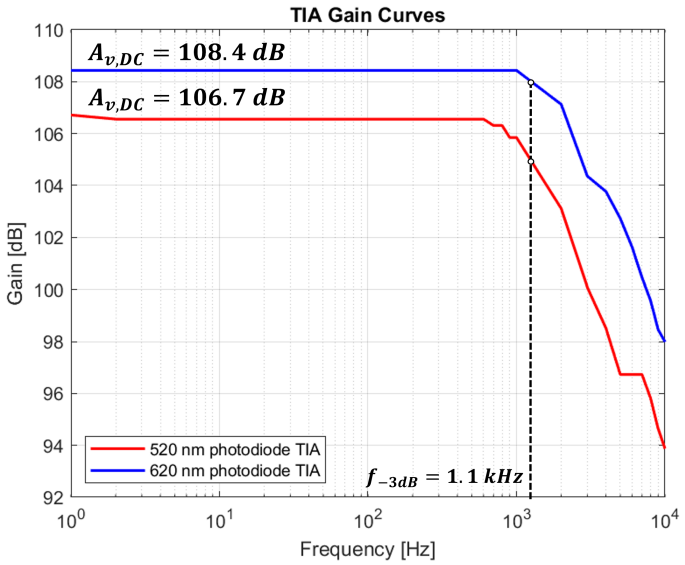

Figure 3.21: Single-ended TIA gain bode plot.

A picture of the testbench used for AFE testing is shown in Figure 3.22.

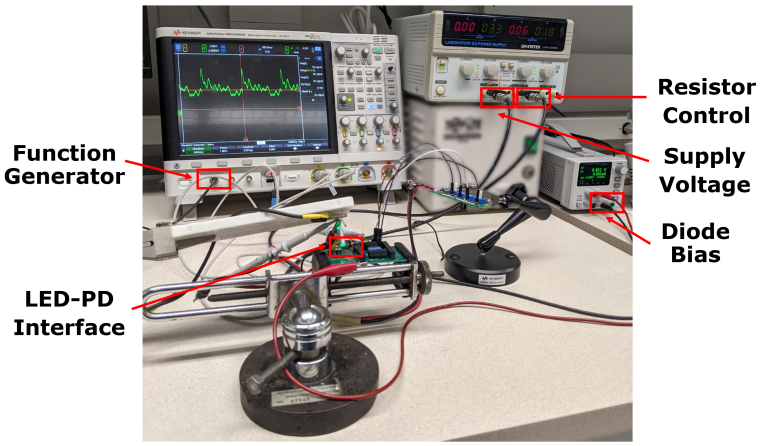

Figure 3.22: Picture of AFE testbench.

3.7 Board Layout

The PCB layout used in this design is shown in Figure 3.24. The board contains four layers; top signal layer, ground plane, supply voltage plane, and bottom signal layer. The majority of the board area is taken up by testpoints added for probing of selected tapeout pads. An SMA connector was included to allow for feeding of an external function generator signal to the active rectifier tapeout.

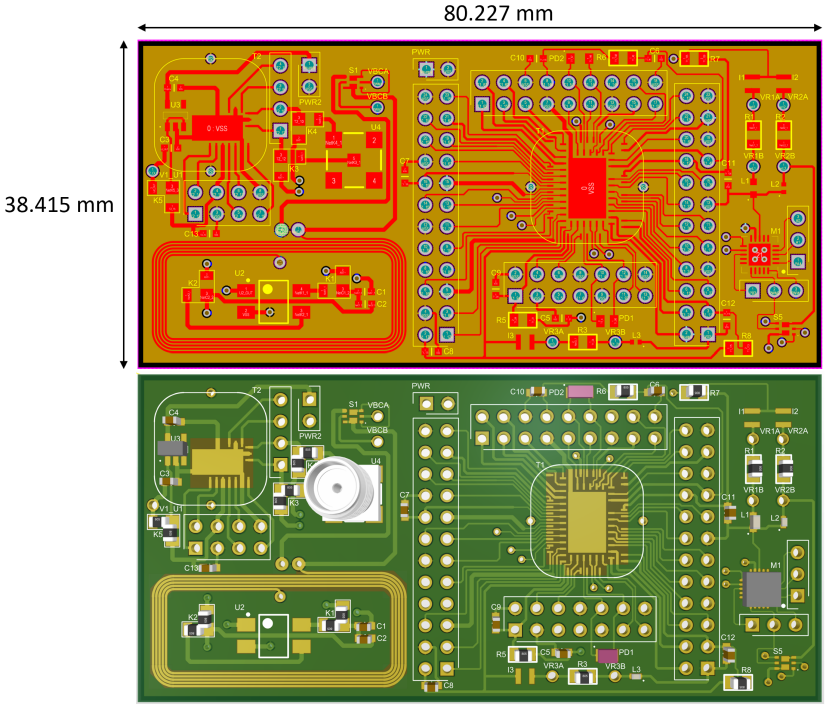

Figure 3.23: PCB layout.

The tapeouts were connected to board pads manually using a wirebonder machine. A wedge bonding technique was used with 25 um gold wire.

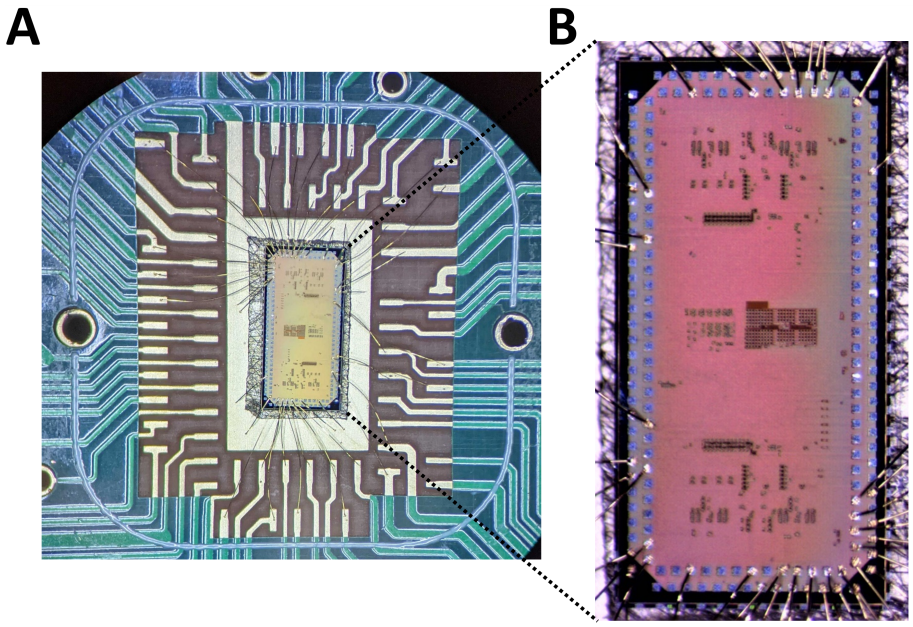

Figure 3.24: (A) View of chip wirebonded to the board. (B) Zoomed in view of the die.

Chapter 4

Conclusion

This thesis outlines the development of a two iterations of a wireless photometry device for the optical stimulation and recording of Ca^{2+} and ACh concentrations in the basal forebrain and hippocampus. Chapter 1 describes the motivation for this project, mainly the collection of quantitative data to substantiate a hypothesis regarding the biological mechanisms that contribute to the onset of neurological conditions. Chapter 2 delves in detail into the system design and testing of a prototype made of discrete components. Chapter 3 follows a similar structure regarding and integrated circuit prototype.

The goal of this research effort was to provide a proof-of-concept with an initial prototype, then optimize the design with an integrated circuit solution. In-vitro testing demonstrated that both prototypes worked as expected in comparison to simulation results. The promising results from these prototype experiments was successfully used in the Humans Frontiers Grant Proposal that will continue to fund future work in this project.

4.1 Future Work

The ICAS lab is planning a third tapeout that will be integrated into the next iteration prototype. Based on the research presented in this thesis, there are a number of design recommendations that can be made. In addition, there are measurements that were not

carried out for the presented prototypes that should be conducted for future prototypes.

Starting of with the design recommendations, the tapeout used for the second prototype was originally made for another application. As a result, the bandwidth and gain were not optimized for a cholinergic signal input. Based on the frequency spectrum of the input signal, the majority of the cholinergic signal power is concentrated below 20 Hz. In addition, the expected signal amplitude is around 1 μA based on the fiber photometry data we acquired. Therefore, a bandwidth of around 50 Hz and a gain of 120-130 dB would attenuate the majority of out-of-band noise while producing a rail-to-rail output for the signal of interest. Another improvement that can be made is with regards to the differential TIA. Typically, the added complexity and power consumption of this topology is justified by the doubling in dynamic range where the output swings from ground up to $2 \cdot VDD$. In contrast, the TIA design used in the tapeout produced a plus and a minus output that swung from common-mode to the positive supply rail and ground respectively. The subsequent differential signal was a rail-to-rail output which can be achieved with a single-ended excitation configuration. The additional benefits of a single-ended excitation include a simpler design that aids in debugging during lab testing. Furthermore, fewer transistors in the design reduces power consumption significantly which is an important parameter in wireless devices. Moving on the optical stimulation stage, in this design a MCU was used to independently control the duty cycle and period of LED driver. For the new prototype, incorporating control of the PWM signal on the chip would be preferred as this would eliminate the need for an external MCU. Furthermore, the justification for the use of the boost converter topology was because the forward voltage of the LED needed to be reached while using a 1.8 V TSMC process node. While this circuit was able to drive the LEDs by dumping stored up current to the LED input node, an issue that was observed was that the LED voltage never went to 0 V. This means that the LED driver is ON continuously which wastes power. For future LED driver circuits, if a boost converter topology is utilized then some method must be devised to discharge this node or reuse the charge to save power. Alternatively, a 3.3 V or 5 V process node

could be used to circumvent the boost converter circuit entirely. Finally, in both prototypes the bleaching was combatted by controlling LED illuminance. Bleaching is an phenomenon where the neuron gets desensitised and stops emitting light when overstimulated. While the approach used is acceptable, a more accurate way of avoiding bleaching is to use a current sense feedback to ensure that the LED illuminance remains constant over long measurement periods, another feature to be incorporated in future prototypes.

Moving on to the future measurements to conduct, the final goal of this project was to design a device capable of being used by research labs to measure cholinergic marker concentrations in the brain of live animal models. To do this, an in-vivo experiment with mice would have to be done. The main barrier to doing such an experiment with the current prototypes was the lack of a shank. The shank allows the LEDs and photodiodes to be implanted in the brain. The design and production of a shank is outside the expertise of the ICAS lab, therefore we would have to collaborate with a third-party lab or company.

References

[1] United Nations, Department of Economic and Social Affairs, and Population Division, "Global and regional trends in population ageing," p. 7, 2020. [Online]. Available: https://www.un.org/development/desa/pd/sites/www.un.org.development.desa.pd/files/files/documents/2020/Jan/un_2019_worldpopulationageing_report.pdf

[2] A. V. Terry and J. J. Buccafusco, "The cholinergic hypothesis of age and alzheimer's disease-related cognitive deficits: Recent challenges and their implications for novel drug development," *J Pharmacol Exp Ther*, vol. 306, no. 3, pp. 821–827, Sept, 2003. [Online]. Available: https://pubmed.ncbi.nlm.nih.gov/12805474/

[3] A. A. Patel, N. McAlinden, K. Mathieson, and S. Sakata, "Simultaneous electrophysiology and fiber photometry in freely behaving mice," vol. 14, p. 148, Feb, 2020. [Online]. Available: https://www.frontiersin.org/article/10.3389/fnins.2020.00148

[4] Y. Jia, Y. Gong, A. Weber, W. Li, and M. Ghovanloo, "A mm-sized free-floating wireless implantable opto-electro stimulation device," vol. 11, no. 6, p. 621, June, 2020. [Online]. Available: https://www.mdpi.com/2072-666X/11/6/621

[5] K. Kampasi, D. F. English, J. Seymour, E. Stark *et al.*, "Dual color optogenetic control of neural populations using low-noise, multishank optoelectrodes," *Microsyst Nanoeng*, vol. 4, no. 1, p. 10, Dec, 2018. [Online]. Available: https://www-nature-com.ezpxy-web-p-u01.wpi.edu/articles/s41378-018-0009-2.pdf

[6] A. Chakravarti, Y. Tsuno, and U. Guler, "Towards a tri-color wireless photometry system for the monitoring of neuronal activity in the basal forebrain and hippocampus," in *IEEE Engineering in Medicine and Biology Society (EMBC 2021)*. [Online]. Available: https://ieeexplore.ieee.org/document/9075881/

[7] Alzheimer's Association, "2021 alzheimer's disease facts and figures," p. 19, 2021. [Online]. Available: https://www.alz.org/media/documents/alzheimers-facts-and-figures.pdf

[8] E. R. Dorsey, A. Elbaz, E. Nichols, F. Abd-Allah *et al.*, "Global, regional, and national burden of parkinson's disease, 1990–2016: a systematic analysis for the global burden of disease study 2016," *The Lancet Neurology*, vol. 17, no. 11, pp. 939–953, Nov, 2018. [Online]. Available: https://www.thelancet.com/journals/laneur/article/PIIS1474-4422(18)30295-3/abstract

[9] B. Plassman, K. Langa, G. Fisher, S. Heeringa *et al.*, "Prevalence of dementia in the united states: The aging, demographics, and memory study," vol. 29, no. 1, pp. 125–132, Nov, 2007. [Online]. Available: https://www.ncbi.nlm.nih.gov/pmc/articles/PMC2705925/

[10] P. Mehta, W. Kaye, J. Raymond, R. Punjani *et al.*, "Prevalence of amyotrophic lateral sclerosis — united states, 2015," vol. 67, no. 46, p. 5, Nov, 2018. [Online]. Available: https://www.cdc.gov/mmwr/volumes/67/wr/pdfs/mm6746a1-H.pdf

[11] A. Kumar, J. Sidhu, A. Goyal, and J. W. Tsao, *Alzheimer Disease*. StatPearls Publishing, Jan, 2021. [Online]. Available: https://www.ncbi.nlm.nih.gov/books/NBK499922/

[12] Leonard E. Jarrad, "On the role of the hippocampus in learning and memory in the rat," *Behavioral and Neural Biology*, vol. 60, no. 1, pp. 9–26, July, 1993. [Online]. Available: http://www.sciencedirect.com/science/article/pii/0163104793906644

[13] F. H. Gage, A. Björklund, U. Stenevi, S. B. Dunnett *et al.*, "Intrahippocampal septal grafts ameliorate learning impairments in aged rats," *Science*, vol. 225, pp. 533–537, Aug, 1984. [Online]. Available: https://pubmed.ncbi.nlm.nih.gov/6539949/

[14] R. T. Bartus, R. L. Dean, B. Beer, and A. S. Lippa, "The cholinergic hypothesis of geriatric memory dysfunction," *Science*, vol. 217, no. 4558, pp. 408–417, Jul, 1982. [Online]. Available: https://pubmed.ncbi.nlm.nih.gov/7046051/

[15] F. Gage and A. Bjorklund, "Cholinergic septal grafts into the hippocampal formation improve spatial learning and memory in aged rats by an atropine-sensitive mechanism," *J Neurosci*, vol. 6, no. 10, pp. 2837–2847, Oct, 1986. [Online]. Available: https://www.ncbi.nlm.nih.gov/pmc/articles/PMC6568784/

[16] T. A. Slotkin, F. J. Seidler, B. J. Crain, J. M. Bell *et al.*, "Regulatory changes in presynaptic cholinergic function assessed in rapid autopsy material from patients with alzheimer disease: implications for etiology and therapy." *PNAS*, vol. 87, no. 7, pp. 2452–2455, April, 1990. [Online]. Available: http://www.pnas.org/cgi/doi/10.1073/pnas.87.7.2452

[17] K. L. Davis, "Cholinergic markers in elderly patients with early signs of alzheimer disease," *JAMA*, vol. 281, no. 15, p. 1401, April, 1999. [Online]. Available: http://jama.jamanetwork.com/article.aspx?doi=10.1001/jama.281.15.1401

[18] H. Dana, B. Mohar, Y. Sun, S. Narayan *et al.*, "Sensitive red protein calcium indicators for imaging neural activity," *eLife*, vol. 5, p. 5, Mar, 2016. [Online]. Available: https://doi.org/10.7554/eLife.12727

[19] M. Jing, Y. Li, J. Zeng, P. Huang *et al.*, "An optimized acetylcholine sensor for monitoring in vivo cholinergic activity," *Nature Methods*, vol. 17, no. 11, pp. 1139–1146, Nov, 2020. [Online]. Available: https://www.nature.com/articles/s41592-020-0953-2

[20] M. Jing, P. Zhang, G. Wang, J. Feng *et al.*, "A genetically encoded fluorescent acetylcholine indicator for in vitro and in vivo studies," vol. 36, no. 8, pp. 726–737. [Online]. Available: https://www.nature.com/articles/nbt.4184

[21] Y. Sych, M. Chernysheva, L. T. Sumanovski, F. Helmchen *et al.*, "High-density multi-fiber photometry for studying large-scale brain circuit dynamics." vol. 16, no. 6, pp. 553–560, June, 2019. [Online]. Available: https://www.proquest.com/docview/2232026433?pq-origsite=primo

[22] G. Paxinos and K. B.J. Franklin, *The Mouse Brain in Stereotaxic Coordinates, second edition.* San Diego: Academic Press, Jul, 2001. [Online]. Available: https://www.worldcat.org/title/mouse-brain-in-stereotaxic-coordinates/oclc/249424773?referer=di&ht=edition

[23] L. Lu, P. Gutruf, L. Xia, D. L. Bhatti *et al.*, "Wireless optoelectronic photometers for monitoring neuronal dynamics in the deep brain," *PNAS*, vol. 115, no. 7, pp. E1374–E1383, Feb, 2018. [Online]. Available: http://www.pnas.org/lookup/doi/10.1073/pnas.1718721115

[24] T. Wang and B. Erhman, "Compensate transimpedance amplifiers intuitively," Texas Instruments, Application Report SBOA055A, March, 2005. [Online]. Available: https://www.ti.com/lit/an/sboa055a/sboa055a.pdf?ts=1639674745731&ref_url=https%253A%252F%252Fwww.google.com%252F

[25] H. Hashemi, "Transimpedance amplifiers (TIA): Choosing the best amplifier for the job," Texas Instruments, Application Report SNOA942A. [Online]. Available: https://www.tij.co.jp/jp/lit/an/snoa942a/snoa942a.pdf

[26] Y. Tsuno, "Calcium ion transient fiber photometry data," E-mail, Dec, 2021.

[27] J. Baker, *CMOS Circuit Design, Layout, and Simulation*, 3rd ed. John Wiley & Sons. [Online]. Available: https://www.wiley.com/en-us/CMOS%3A+Mixed+Signal+Circuit+Design%2C+2nd+Edition-p-9780470290262

[28] S. Song, M. Konijnenburg, R. v. Wegberg, J. Xu *et al.*, "A 769 w battery-powered single-chip SoC with BLE for multi-modal vital sign monitoring health patches," vol. 13, no. 6, pp. 1506–1517, Dec, 2019. [Online]. Available: https://ieeexplore.ieee.org/document/8854984

[29] I. Costanzo, D. Sen, and U. Guler, "An integrated readout circuit for a transcutaneous oxygen sensing wearable device," in *IEEE Custom Integrated Circuits Conference (CICC 2020)*, pp. 1–4. [Online]. Available: https://ieeexplore.ieee.org/document/9075881/

[30] K.-W. Yao, C.-S. Alex Gong, S.-C. Yang, and M.-T. Shiue, "Design of a neural recording amplifier with tunable pseudo resistors," Sept, 2011. [Online]. Available: https://ieeexplore.ieee.org/document/6085119

Appendix A

TIA Stability Analysis Plots

Feedback Stability Analysis Plots:

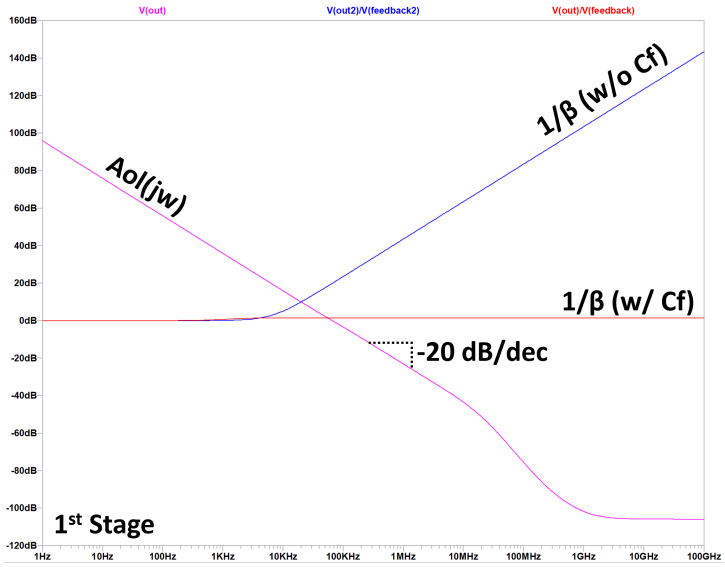

Figure A.1: 520 nm photodiode first-stage TIA open-loop response and feedback response with and without the feedback capacitor.

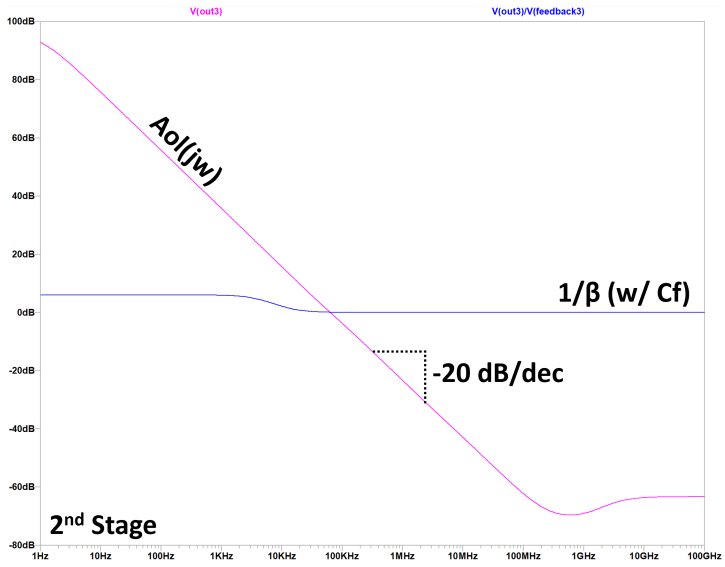

Figure A.2: 520 nm photodiode second-stage TIA open-loop response and feedback response with and without the feedback capacitor.

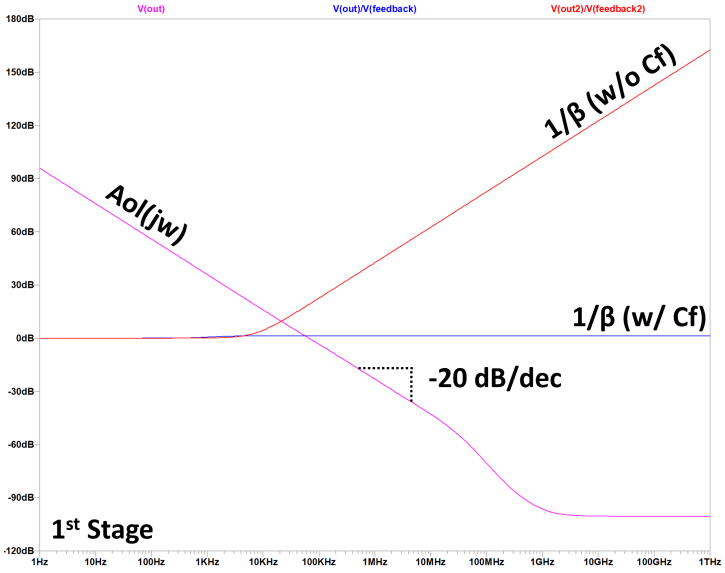

Figure A.3: 620 nm photodiode first-stage TIA open-loop response and feedback response with and without the feedback capacitor.

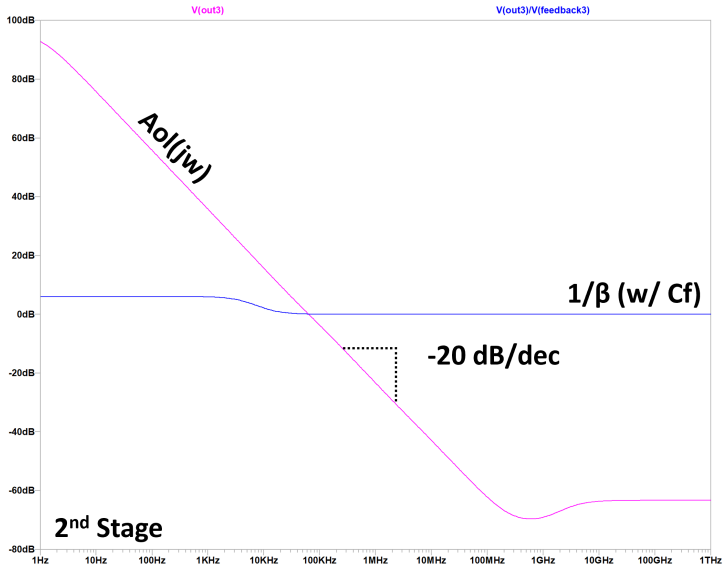

Figure A.4: 620 nm photodiode second-stage TIA open-loop response and feedback response with and without the feedback capacitor.

Transient Stability Analysis Plots:

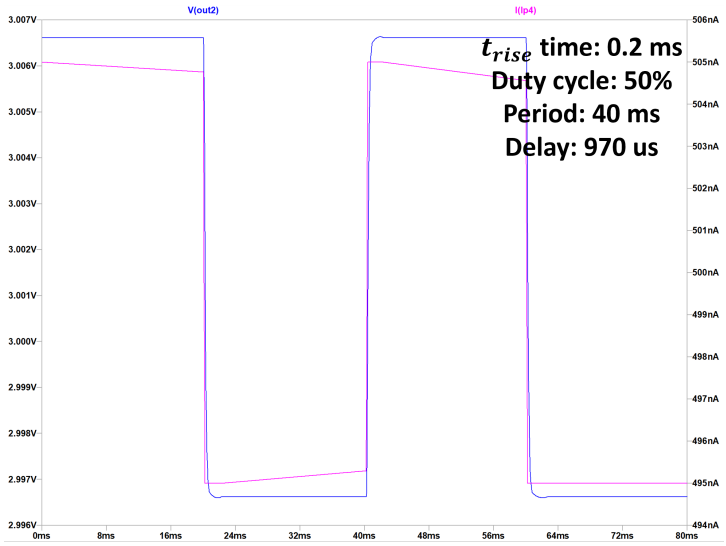

Figure A.5: 520 nm photodiode first-stage TIA transient square wave input and output plot.

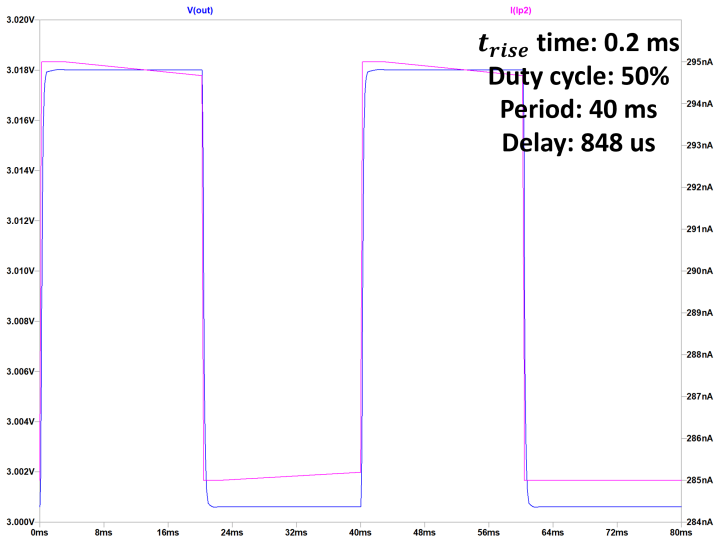

Figure A.6: 620 nm photodiode first-stage TIA transient square wave input and output plot.

AC Stability Analysis Plots:

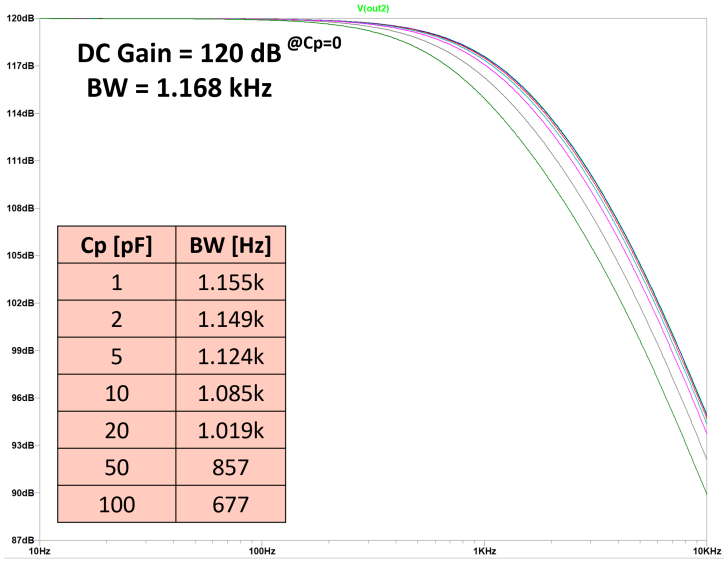

Cp [pF]	BW [Hz]
1	1.155k
2	1.149k
5	1.124k
10	1.085k
20	1.019k
50	857
100	677

Figure A.7: 520 nm photodiode first-stage TIA AC stability plot when parasitic capacitance is swept.

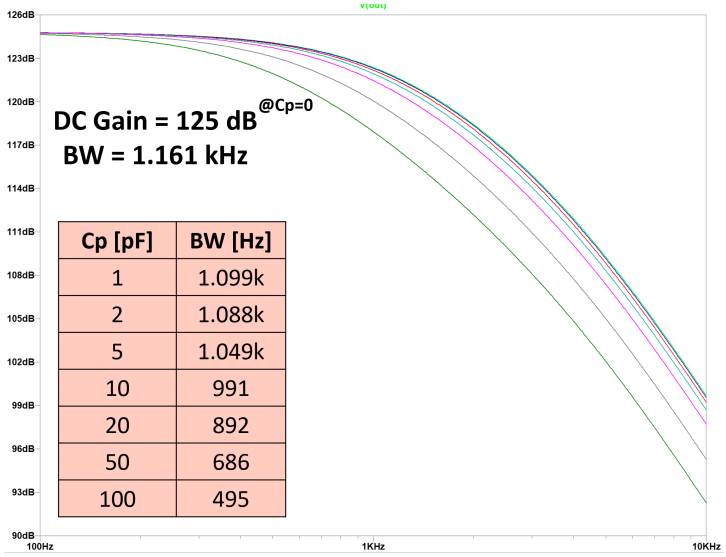

Cp [pF]	BW [Hz]
1	1.099k
2	1.088k
5	1.049k
10	991
20	892
50	686
100	495

Figure A.8: 620 nm photodiode first-stage TIA AC stability plot when parasitic capacitance is swept.

Appendix B

EMBS Conference Paper

Towards a Tri-Color Wireless Photometry System for the Monitoring of Neuronal Activity in the Basal Forebrain and Hippocampus

Aatreya Chakravarti[†], Yusuke Tsuno[§], and Ulkuhan Guler[†]
[†]Department of Electrical and Computer Engineering, Worcester Polytechnic Institute, Worcester, MA 01609 USA
[§]Department of Integrative Neurophysiology, Kanazawa University, Kanazawa, Ishikawa 920-8640, Japan
Email: achakravarti@wpi.edu, tsuno@med.kanazawa-u.ac.jp, and uguler@wpi.edu

***Abstract*— Healthy cholinergic function is important for brain function, and disruption of the system is thought to be the cause of dementia, including Alzheimer's disease. The 'Cholinergic Hypothesis' theorizes that cognitive decline is due disruption of the cholinergic system, defined by the low concentration of neurotransmitters such as acetylcholine (ACh) and neurotransmitter-releasing elements such as calcium ions (Ca^{2+}). The ability to measure ACh and Ca^{2+} concentrations enables researchers to make inferences on the relationship between these indicators that play a role in the onset of neurological conditions. Current commercial devices have one or more of the following limitations: i) they are tethered making it difficult to verify in naturally behaving animal subjects, ii) they are capable of only measuring a single indicator at any given time, or iii) they have multiple shanks that penetrate the cortex. We propose a tri-color miniaturized photometry system capable of optically stimulating indicators in neurons located in the hippocampus and basal forebrain and optically reading the neurons' response. The resulting device has an average gain of 123 dB and a power consumption of 29 mW, comparable to other state-of-the-art devices.**

I. Introduction

According to United Nations, the percentage of the world population aged 65 and older has jumped from 5% in 1990 to ∼10% in 2020 [1]. The same source estimates that this number is going to increase to ∼18% by 2050. With age comes higher susceptibility to developing neurological conditions such as dementia, Parkinson's disease and Alzheimer's disease (AD). According to a systematic review of data published in the 2021 Alzheimer's Association report, of the 6.2 million Americans with AD aged 65 or older, 27.6% are 65-74, 36.1% are 75-84, and 36.4% are 85+ years of age [2].

Researchers have attempted to identify the correlation between age and increase in AD prevalence. The 'Cholinergic Hypothesis' explains the acceleration of cognitive decline symptoms such as progressive memory loss in elderly individuals due to a decline in cholinergic function [3], as shown in Fig. 1. Cholinergic dysfunction is defined as a disruption in the cholinergic neurotransmitter pathway indicated by low concentrations of various neurotransmitters and the elements that release these neurotransmitters [3].

Verification of these claims are based on post-mortem analysis of brain tissue from AD patients [4], [5] or indirect behavioral evidence collected from live animal models [6], [7]. The former analysis is unreliable due to case-to-case variability in tissue deterioration based on when the autopsy was carried out post-mortem. The latter analysis fails to provide direct evidence of cholinergic input through any quantitative measure of the neurotransmitter pathway disruption. Quantitative measurement of cholinergic input in live animal models can be done by directly measuring the hippocampal concentration of acetylcholine (ACh), a cholinergic neurotransmitter, in freely-moving animals. In addition, measurements with live animal models allows for collection of data in a range of ages allowing researchers to correlate age and cholinergic function. Measurements of concentration are enabled by indicators that cause cholinergic neurons to fluoresce when optically stimulated with a specific wavelength. The fluorescence intensity is dependent on the concentration of the targeted neurotransmitters or neurotransmitter-releasing elements.

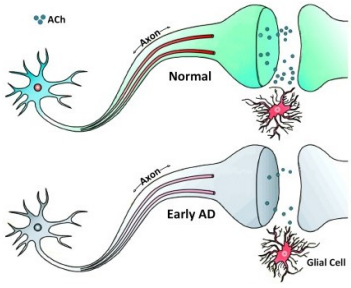

Fig. 1. Illustration of cholinergic neurons in healthy versus early AD patients, influenced by [8]

To make direct measurements, recent studies present wireless photometry systems that measure the concentration of calcium ions (Ca^{2+}), an element that triggers cholinergic neurotransmitter release [9], [10]. Although these systems are wireless and thereby overcome the challenges of measuring naturally behaving animals, none of these systems are capable of measuring both ACh and Ca^{2+}. This feature is advantageous for three reasons: i) measuring two cholinergic markers will provide stronger evidence of cholinergic function or dysfunction compared to measuring only one, ii) the role of ACh in cognitive decline symptoms can be quantitatively explored which is not possible with current commercial devices that are designed to measure only Ca^{2+},

*This work was partially supported by Japan Agency for Medical Research and Development (AMED).

TABLE I
SIGNALS OF INTEREST STIMULATION AND EMISSION WAVELENGTHS

Neural Signal	Stimulation Wavelength	Emission Wavelength
Ca^{2+} Sensing	525-575 nm – yg	620-660 nm – o
ACh Sensing	465-480 nm – pb	510-530 nm – bg
ACh_{iso} Sensing	405 nm - bv	510-530 nm – bg

yg = yellow-green, pb = pure blue, bv = blue-violet, o = orange, bg = blue-green

and iii) the correlation between ACh and Ca^{2+} can be better understood.

In this paper, a tri-color photometry system capable of optically stimulating and recording multiple wavelengths will be presented. The indicators for ACh and Ca^{2+} sensing are GCaMP [11] and RCaMP [12], respectively. The 470 nm wavelength is used to optically stimulate the ACh indicators in the hippocampus and the 560 nm wavelength performs the same function for the Ca^{2+} indicators in neurons located in the basal forebrain. The 405 nm wavelength is used to measure the ACh isosbestic (ACh_{iso}) signal that does not change during the recording period. Changes in the ACh_{iso} signal can be used as a reference to remove noise from the ACh and Ca^{2+} recordings, such as DC drift from motion artifact.

The motivation for such a device in the long-run is decoding the human brain's underlying mechanisms that cause cognitive decline and a possibility to open up a new venue for surrogate methods that can provide noninvasive personalized monitoring of cognitive decline in patients, specifically in relation to the memory deficits and other cholinergic hippocampus-specific functions. Section II elaborates on the proposed system design. Section III describes the measurement environment, interprets the measurement results, and compares this work to other state-of-the-art systems before the concluding remarks.

II. SYSTEM DESIGN

The wireless photometry device performs two distinct functions; the first function is optical stimulation of indicators, and the second function is reading the light emitted by the stimulated indicators. Referencing Fig. 2, the light emitting diode (LED) stimulation and control stage carry out the first function, and the transimpedance stage performs the second function.

A. LED Stimulation and Control Stage

In this stage, the microcontroller unit (MCU) drives each of the LEDs so that the appropriate indicators can be stimulated and three distinct neural signals can be recorded. The stimulation and emission wavelengths of each signal are given in Table I. In addition to ACh and Ca^{2+} sensing, the device also senses an ACh_{iso} signal that can be used as a baseline control.

The MCU directly drives the LEDs as opposed to using a dedicated LED driver because the chosen MCU can source up to 40 mA from each I/O pin, exceeding LED current drive

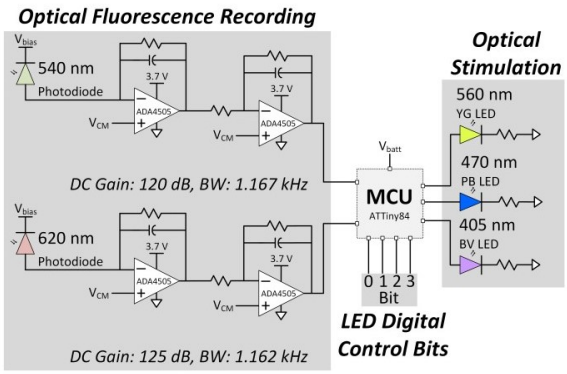

Fig. 2. Block diagram of the tri-color wireless photometry system.

requirements. Each of the LEDs is sourced by separate I/O pins to allow for multiplexing flexibility that can be set in the MCU code. For the test setup presented in this paper, each LED is stimulated at 40 Hz with a 4% duty cycle. Additionally, the ACh and ACh_{iso} signal emission are at the same wavelength; therefore, the 405 and 470 nm LEDs are time-multiplexed so that the photodiode (PD) can distinguish between the two signals.

Finally, the user control of LED illuminance has been added to the device. This is an important feature because excessive LED brightness can lead to a loss of responsivity in the ACh and Ca^{2+} indicators, an effect called bleaching. To control the LEDs' illuminance, four bits have been allocated that can be set to a high (VCC) or low (GND) voltage. The corresponding four-bit binary code ranges from 0000 to 1111. The MCU will read the first two bits to select the LED. 00 selects the 560 nm LED, 01 selects the 470 nm LED, and 10 selects the 405 nm LED. The last two bits will set the brightness to four pre-defined levels. The illuminance levels are set in the MCU code and can be modified.

B. Recording Stage

In this stage, the light emitted by the neurons strikes the PD's active area. As a result, photocurrent that is proportional to the amount and the illuminance of the incident light is generated by the PDs. The photocurrent is then converted into voltage that can be sampled by the MCU. A transimpedance amplifier (TIA) carries out the conversion. The design has two TIA circuits: the first circuit is connected to a PD sensitive to 620 nm (Ca^{2+} sensing), and the second one to a PD sensitive to 520 nm (ACh and ACh_{iso} sensing). Due to the time multiplexing of the ACh and ACh_{iso} stimulation LEDs, the two signals are distinguishable. Following the TIA stage, a low-pass filter is used to attenuate further noise outside the ~1 kHz bandwidth and invert the TIA output.

TIA stability is of crucial importance to this design. To ensure its stability, SPICE simulations were carried out. We performed the following three analyses: i) Open-loop gain (A_{OL}) and feedback factor (β) AC analysis to ensure that the feedback pole does not degrade the phase margin, which is true if the A_{OL} plot slope is -20 dB/dec before and after

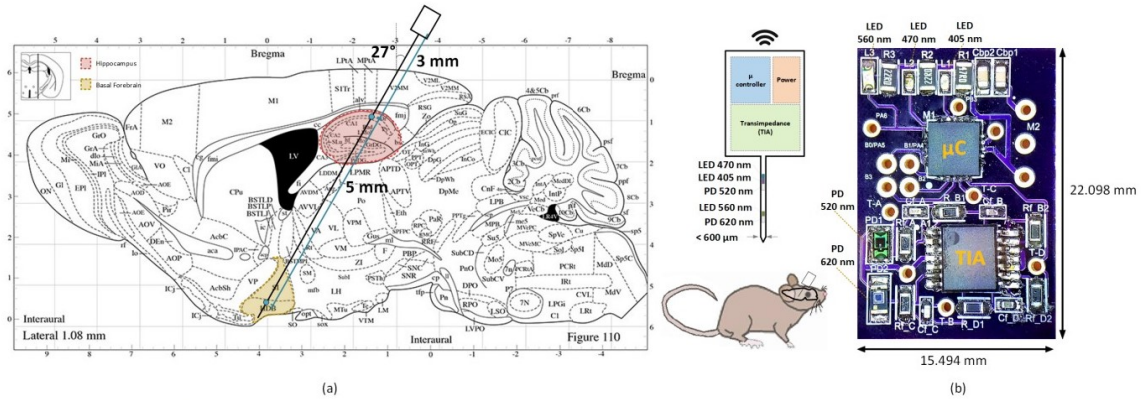

Fig. 3. (a) Parasaggital mouse brain slice with the highlighted hippocampus (red) and basal forebrain (yellow). (b) Tri-color photometry device photo.

intersecting the plot of $1/\beta$. ii) Transient analysis with an input small-signal ($\sim$ 5 mV_{pp}) square wave to observe any overshoot or ringing in the output, a sign of instability. iii) Changing the parasitic capacitance value across a range (1 pF to 100 pF) to see the effect on bandwidth. Choosing the feedback capacitor's value can affect the TIA circuit stability due to the number of trade-offs involved: a) The capacitor value needs to be high enough to compensate for the TIA. b) The value needs to be much greater than typical printed-circuit-board (PCB) parasitic capacitance values, generally in the hundreds of fF range. When trying to meet these criteria, the value cannot be substantially large because this will affect the signal settling time. c) The capacitor value should achieve the required bandwidth without making the feedback resistor value large.

C. Shank Positioning

The device presented in this paper does not consist of a shank. However, in future iterations of this device, a shank will be included. Due to this system's unique tri-color optical stimulation and recording capabilities, shank placement is an essential aspect of the design.

To measure both ACh and Ca^{2+} in the hippocampus and basal forebrain, the shank will be inserted at approximately a 27° angle perpendicular to the surface of the animal's brain, as shown in Fig. 3a (based on the Mouse Brain Atlas [13]).

Two groups of LEDs and PDs will be located at a precise distance on the shank relative to the headstage to optically stimulate and record appropriate parts of the brain. The 405 nm and the 470 nm LEDs and the 520 nm PD will be placed 3 mm from the headstage such that they are in proximity to the hippocampus to stimulate and record ACh and the ACh_{iso} signal. The 560 nm LED and 620 nm PD will be placed 8 mm from the headstage near the basal forebrain to stimulate and record Ca^{2+} signals.

III. Measurement Results

A PCB, depicted in Fig. 3b, hosts the tri-color photometry circuitry, also equipped with LEDs and PDs. The size of the PCB is $\sim$ 15.5 $\times$ 22.1 mm^2. Once the shank gets its final form, the LEDs and PDs with bare active areas will position on the shank reducing the circuit area on the PCB. A LiPo battery is attached to the system

To characterize the LED control stage, we used the Thorlabs spectrometer to measure the relative intensity of each LED when set to each bit code from 00 to 11. The relative intensity increased almost linearly with each increase in bit code value, as shown in Fig. 4a. For the PDs, prior to measurement the components were calibrated with a power meter to ensure that the correlation between light intensity to forward current matches the manufacturers datasheet.

To mimic the real emission of neurons, we have used real Ca^{2+} transient brain data collected using a fiber photometry system. This data was uploaded to an arbitrary function generator and used to drive two LEDs with wavelengths of 520 and 620 nm, the characteristic wavelengths of emission from the neurons in the hippocampus and basal forebrain, respectively. The light emitted from these LEDs was made incident to the PDs via an aluminum foil conduit to reduce ambient light interference. The voltage at the output of the recording stages was then observed. An illustration of the test setup is shown in Fig. 4b.

The blue waveform in Fig. 4c is a 1.6-second portion of the total 11 minutes of data measured by the fiber photometry system, measured at the output of the arbitrary function generator. The green and red waveforms were measured at the outputs of transimpedance amplifiers connected to the 520 and 620 nm PDs, respectively. These signals represent voltages converted from photocurrent generated by each PD in response to the light incident on it from the LEDs. As can be seen, the brain data from the LEDs, representing the emitted light of neurons with optically stimulated indicators, was replicated at the output of each transimpedance stage, demonstrating a proof-of-concept for the recording stage.

A comparison of the proposed tri-color miniaturized photometry system specifications with other state-of-the-art printed circuit board systems is presented in Table II. The systems with integrated circuits have been excluded for a fair comparison. This system is distinguished from other recent work due to the multi-color stimulation functionality. [14] presents a dual-color stimulation device, however, the

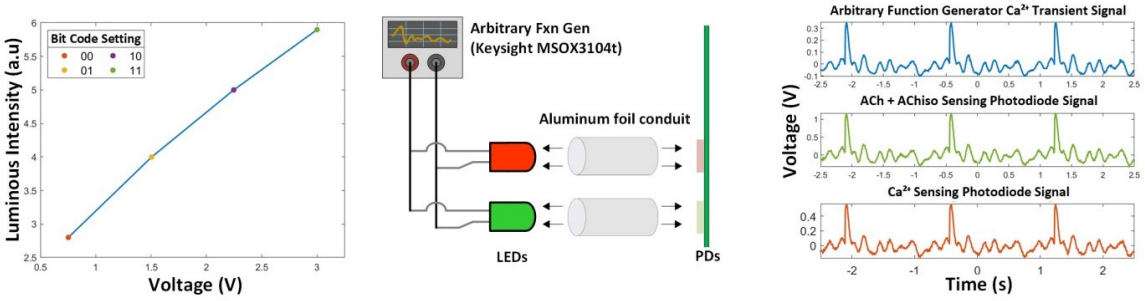

Fig. 4. (a) A plot of bit code value versus relative luminous intensity of 560 nm LED. (b) Illustration of testing procedure for the transimpedance stage. (c) AFG Ca^{2+} transient signal and measured PD signals.

TABLE II
COMPARISON WITH STATE-OF-THE-ART SYSTEMS

Parameters	2018 [9]	2020 [16]	2018 [14]	2021 [This Work]
Power Consumption (mW)	24	15	320	29
Measurement Gain (dB)	NA	50	NA	120-124
Headstage LxW (mm)	7x6.5	7x12	22x14	22.1x15.5
Shank LxW (mm)	0.35x0.15	9x1	5x0.07	NA
Weight (g)	0.5	1.07	1.5	<1
No. of colors	1	1	2	3
No. of shanks	1	1	4	1
No. of channels	1	1	32	2
LED Wavelengths	470	475	405 635	405 470 560

device has multiple shanks that can cause greater tissue damage in contrast to a single shank design. [15] presented a single shank device offering dual-color stimulation, but this device can only simultaneously stimulate one-color at any given time. In addition to this unique feature, this work also has more than double the gain of other systems in the measurement stage, which is beneficial due to the small amplitude of the brain signals being recorded. Lastly, the weight of the device is less than 1 g which is comparable to the weight of other systems. Due to the lack of shank, the device dimensions are larger because the three LEDs and two PDs are placed on the headstage. The power consumption of 29 mW was measured while time multiplexing the three LEDs with a per-LED stimulation frequency of 40 Hz.

IV. CONCLUSION

In this paper, a tri-color wireless photometry system was presented. The device is capable of recording ACh, ACh_{iso}, and Ca^{2+} concentrations. The ability to measure the concentration of more than one biomarker on a single device is beneficial because it will allow physicians and researchers to make conclusions on the role of both ACh and Ca^{2+} in accelerating neurological conditions in elderly patients. Some of the requirements needed to make this system applicable for testing in vivo still need to be added. For one, a shank with appropriate stiffness needs to be designed. In addition, to remove the need for wires of any kind, wireless data transmission and power are crucial. For both of these, a board antenna needs to be added to the device. Finally, miniaturizing the board and reducing power consumption are continuous goals for any wearable system.

REFERENCES

[1] United Nations, Department of Economic and Social Affairs, and Population Division, "Global and regional trends in population ageing," p. 7, 2019. [Online]. Available: https://www.un.org/development/desa/pd/sites/www.un.org.development.desa.pd/files/files/documents/2020/Jan/un2019worldpopulationageingreport.pdf

[2] Alzheimer's Association, "2021 alzheimer's disease facts and figures," p. 19, 2021. [Online]. Available: https://www.alz.org/media/documents/alzheimers-facts-and-figures.pdf

[3] R. T. Bartus *et al.*, "The cholinergic hypothesis of geriatric memory dysfunction," *Science*, vol. 217, no. 4558, pp. 408–417, 1982.

[4] T. A. Slotkin *et al.*, "Regulatory changes in presynaptic cholinergic function assessed in rapid autopsy material from patients with alzheimer disease: implications for etiology and therapy." *PNAS*, vol. 87, no. 7, pp. 2452–2455, April, 1990.

[5] K. L. Davis, "Cholinergic markers in elderly patients with early signs of alzheimer disease," *JAMA*, vol. 281, no. 15, p. 1401, April, 1999.

[6] F. Gage *et al.*, "Cholinergic septal grafts into the hippocampal formation improve spatial learning and memory in aged rats by an atropine-sensitive mechanism," *J Neurosci*, vol. 6, no. 10, pp. 2837–2847, Oct, 1986.

[7] F. H. Gage *et al.*, "Intrahippocampal septal grafts ameliorate learning impairments in aged rats," *Science*, vol. 225, pp. 533–537, Aug, 1984.

[8] A. V. Terry *et al.*, "The cholinergic hypothesis of age and alzheimer's disease-related cognitive deficits: Recent challenges and their implications for novel drug development," *J Pharmacol Exp Ther*, vol. 306, no. 3, pp. 821–827, Sept, 2003.

[9] L. Lu *et al.*, "Wireless optoelectronic photometers for monitoring neuronal dynamics in the deep brain," *PNAS*, vol. 115, no. 7, pp. E1374–E1383, Feb, 2018.

[10] Y. Jia *et al.*, "A trimodal wireless implantable neural interface system-on-chip," *IEEE Trans Biomed Circuits Syst*, vol. 14, no. 6, pp. 1207–1217, Dec, 2020.

[11] M. Jing *et al.*, "An optimized acetylcholine sensor for monitoring in vivo cholinergic activity," *Nature Methods*, vol. 17, no. 11, pp. 1139–1146, Nov, 2020.

[12] H. Dana *et al.*, "Sensitive red protein calcium indicators for imaging neural activity," *eLife*, vol. 5, p. 5, 2016.

[13] F. P. G *et al.*, *The Mouse Brain in Stereotaxic Coordinates, second edition*. San Diego: Academic Press, 2003.

[14] K. Kampasi *et al.*, "Dual color optogenetic control of neural populations using low-noise, multishank optoelectrodes," *Microsyst Nanoeng*, vol. 4, no. 1, p. 10, Dec, 2018.

[15] K. Kampasi *et al.*, "Fiberless multicolor neural optoelectrode for in vivo circuit analysis," *Sci Rep*, vol. 6, no. 1, p. 30961, 2016-11.

[16] E. S. Edward *et al.*, "A closed-loop optogenetic stimulation device," *Electronics*, vol. 9, no. 1, p. 96, Jan, 2020.